Exemplary merging clusters: Weak-lensing and X-ray analysis of the double radio relic, merging galaxy clusters MACS J1752.0+4440 and ZWCL 1856.8+6616

Finner, K.; HyeongHan, K.; Jee, M.J.; Wittman, D.; Forman, W.R.; Weeren, R.J. van; … ; Jones, C.

Citation

Finner, K., HyeongHan, K., Jee, M. J., Wittman, D., Forman, W. R., Weeren, R. J. van, … Jones, C. (2021). Exemplary merging clusters: Weak-lensing and X-ray analysis of the double radio relic, merging galaxy clusters MACS J1752.0+4440 and ZWCL 1856.8+6616. *The Astrophysical Journal*, *918*(2). doi:10.3847/1538-4357/ac0d00

Draft version November 23, 2021
Typeset using LATEX **twocolumn** style in AASTeX62

arXiv:2010.02226v1 [astro-ph.GA] 5 Oct 2020

Exemplary Merging Clusters: Weak-lensing and X-ray Analysis of the Double Radio Relic Merging Galaxy Clusters MACS 1752.0+4440 and ZWCL 1856.8+6616

Kyle Finner,[1] Kim Hyeonghan,[1] M. James Jee,[1,2] David Wittman,[2] William R. Forman,[3]
Reinout J. van Weeren,[4] Nathan R. Golovich,[5] William A. Dawson,[5] Alexander Jones,[6] and
Francesco de Gasperin[6]

[1]*Department of Astronomy, Yonsei University, 50 Yonsei-ro, Seoul 03722, Korea*
[2]*Department of Physics, University of California, Davis, One Shields Avenue, Davis, CA 95616, USA*
[3]*Smithsonian Astrophysical Observatory, Harvard-Smithsonian Center for Astrophysics, 60 Garden St., Cambridge, MA 02138, USA*
[4]*Leiden Observatory, Leiden University, PO Box 9513, 2300 RA Leiden, The Netherlands*
[5]*Lawrence Livermore National Laboratory, 7000 East Ave., Livermore, CA 94550, USA*
[6]*Hamburger Sternwarte, University of Hamburg, Gojenbergsweg 112, Hamburg 21029, Germany*

ABSTRACT

The investigation of radio relic merging galaxy clusters is strengthening our understanding of the formation and evolution of galaxy clusters, the nature of dark matter, the intracluster medium, and astrophysical particle acceleration. Each merging cluster provides only a single view of the cluster formation process and the variety of merging clusters is vast. Clusters hosting double radio relics are rare and extremely important because they allow tight constraints on the merger scenario. We present a weak-lensing and X-ray analysis of MACSJ1752.0+4440 and ZWCL1856.8+6616, two double radio relic merging galaxy clusters. Our weak-lensing mass estimates show that each cluster is a major merger with approximately 1:1 mass ratio. The total mass of MACSJ1752.0+4440 (ZWCL1856.8+6616) is $M_{200} = 14.7^{+3.8}_{-3.3} \times 10^{14}$ $M_\odot$ ($M_{200} = 2.4^{+0.9}_{-0.7} \times 10^{14}$ $M_\odot$). We find that these two clusters have comparable features in their weak lensing and gas distributions, even though the systems have vastly different total masses. From the likeness of the X-ray morphologies and the remarkable symmetry of the radio relics, we propose that both systems underwent nearly head-on collisions. However, revelations from the hot-gas features and our multiwavelength data analysis suggest that ZWCL1856.8+6618 is likely at a later merger phase than MACSJ1752.0+4440. We postulate that the SW radio relic in MACSJ1752.0+4440 is a result of particle re-acceleration.

Keywords: gravitational lensing — dark matter — cosmology: observations — X-rays: galaxies: clusters — galaxies: clusters: individual (MACS 1752.0+4440 ZWCL 1856.8+6616) — galaxies:

1. INTRODUCTION

Galaxy clusters gain mass primarily by mergers with other galaxy clusters and groups. The most energetic of these events occurs when two galaxy clusters undergo a major merger. Major cluster mergers are ideal laboratories to study high energy astrophysics such as the nature of dark matter and particle acceleration. However, because galaxy clusters are at the high-mass end of the hierarchical formation of the large scale structure, major cluster mergers are rare.

An indication of a merging event can be detected in the intracluster medium (ICM). Emitting thermal bremsstrahlung radiation at X-ray wavelengths, the ICM of merging clusters tends to show a disturbed morphology that is elongated along the merger axis. The elongation is caused by the hydrodynamical properties of the ICM and is observed in some famous merging clusters such as the Bullet cluster (Markevitch et al. 2004), the Toothbrush cluster (Ogrean et al. 2013b), and the Sausage cluster (Ogrean et al. 2013a). Further investigation with state-of-the-art X-ray telescopes can reveal finer details that trace past merging events

Corresponding author: M. James Jee
mkjee@yonsei.ac.kr

kylefinner@gmail.com

such as stripped gas, cold fronts, sloshing, and shocks (Markevitch & Vikhlinin 2007; Ghizzardi et al. 2010). In rare cases, where the ram-pressure force on one ICM from the other exceeds the gravitational force, the ICM can dissociate from the dark matter (e.g. Bradač et al. 2008; Dawson et al. 2012; Jee et al. 2012; Randall et al. 2016). The projected offset is maximized in clusters that are merging in the plane of the sky.

A primary indicator of a cluster merger is the detection of a shock. Shocks form when the collision velocity of the merging clusters exceeds the sound speed of the ICM. Investigating ∼2:1 mass ratio mergers in cosmological simulations, Ha et al. (2018) specified that two types of shocks can form during a cluster merger. First, as the ICM from each cluster begins to interact, tangential shocks form and propagate tangential to the merger axis (e.g. Gu et al. 2019). Then, near pericenter passage, axial shocks form and propagate ahead of the clusters along the merger axis. Axial shocks are also referred to as bow shocks (Ricker 1998; Sarazin 2002; Markevitch et al. 2002) because of their location ahead of the cluster. The geometry of these shocks can be used to constrain the collision axis of the merger.

Merger shocks are observed in X-ray as a discontinuity in the ICM surface brightness or a jump in temperature from the pre- to the post-shock region. However, the detection of shocks in X-ray wavelengths is hampered by the low brightness of the ICM outside the cluster core. Fortunately, shocks can also be detected at radio frequencies. Radio relics are produced by synchrotron emission from charged particles that are accelerated in merger induced shocks (for reviews of radio relics see Feretti et al. 2012; van Weeren et al. 2019) by diffusive shock acceleration (DSA; Bell 1978; Drury 1983; Malkov & Drury 2001). Radio relics tend to be megaparsec in size and are often found on the periphery of merging clusters. The number of clusters hosting radio relics is about 70, which makes them much rarer than merging clusters (for a list see van Weeren et al. 2019). One reason for the rarity is because axial shocks that face the observer have low surface brightness (Skillman et al. 2013). Therefore, radio relics are preferentially found in mergers that are occurring near the plane of the sky (Golovich et al. 2019a). Another contributor to their rarity may be the poor acceleration efficiency of DSA in weak shocks (Kang & Jones 2005; Botteon et al. 2020). To overcome the poor acceleration efficiency of DSA, the re-acceleration model (Kang & Ryu 2011; Kang et al. 2012; Pinzke et al. 2013), where a population of non-thermal seed electrons is re-accelerated by the shock, may be required. Evidence for particle re-acceleration has been compounding recently with clusters such as PLCKG287.0+32.9 (Bonafede et al. 2014) and Abell 3411 (van Weeren et al. 2017). In the latter study, a connection between a cluster radio galaxy and the radio relic was found.

The rarest of the relic phenomena are double relics that are equidistant from the cluster center. As explained in van Weeren et al. (2019), double radio relics are defined as shocks formed from a single merger event. Having two probes of the same merging event is an advantage that can be used to put tight constraints on the merger scenario. To date, about 12 double radio relic clusters have been identified. The two clusters that are presented in this work are double radio relic clusters.

The Merging Cluster Collaboration[1] is reconstructing the collisions of radio relic merging galaxy clusters to investigate the physics of galaxy clusters. An overview of the merging cluster sample can be found in Golovich et al. (2019b). We are utilizing multiwavelength data to probe the dark matter, ICM, and galaxies so that the components of the merger can be meticulously modeled. We rely on weak lensing (WL) to characterize the mass distributions and estimate subcluster masses in these disturbed systems. The masses that we derive from WL are crucial inputs to our merger simulations (Lee et al. 2020). In this paper, we present the first WL analysis of the double radio relic clusters: MACSJ1752.0+4440 (MACS1752) and ZWCL1856.8+6616 (ZWCL1856).

MACS1752 (z=0.365) was discovered in the Massive Cluster Survey (Ebeling et al. 2001). Edge et al. (2003) found it to be a radio bright cluster through a joint analysis of the Westerbork (WSRT) Northern Sky Survey (Rengelink et al. 1997) and ROSAT All-Sky Survey Bright Source Catalog (Voges et al. 1999). Follow-up WSRT observations in L and S band (van Weeren et al. 2012) revealed that MACS1752 is a merging galaxy cluster with double, megaparsec-sized radio relics and a radio halo. The radio study measured the largest linear size (LLS) of the NE relic to be 1.35 Mpc and the SW relic to be 0.86 Mpc. Integrated spectral indices of the relics were reported as $-1.16^{+0.03}_{-0.03}$ in the NE and $-1.10^{+0.05}_{-0.05}$ in the SW. Bonafede et al. (2012) confirmed the presence of the two radio relics and radio halo in Giant Metrewave Radio Telescope (GMRT) observations. Setting the midpoint between the X-ray brightness peaks as the cluster center, they estimated the projected distance to the relics to be 1.13 Mpc and 0.91 Mpc to the NE and SW, respectively. Joining the GMRT and WSRT observations, Bonafede et al. (2012) measured consistent integrated spectral indices

---

[1] http://www.mergingclustercollaboration.org/

and reported injection spectral indices of ~0.6 and 0.8 and Mach numbers of 4.6 and 2.8 for the NE and SW relics, respectively. Both relics were shown to have polarization peaking at ~40%. They found a spectral index of -1.33 ± 0.07 for the radio halo. Interestingly, they note that the NE relic shows a clear width-wise spectral steepening, a telltale sign of a merger origin of the radio emission, that resembles the steepening found in CIZAJ2242.8+5301 (the Sausage cluster). The Sunyaev-Zel'dovich effect (SZE) mass of the cluster is estimated to be $M_{500} = 6.7^{+0.4}_{-0.5} \times 10^{14}$ M$_\odot$ from Planck Collaboration et al. (2016). MACS1752 has also been the subject of numerical simulations in order to investigate the efficiency of electron and proton acceleration in merger shocks (Vazza et al. 2015) as well as to constrain the efficiency of cosmic ray acceleration (Vazza et al. 2016). In the latter study, a cosmological zoom simulation is presented that reproduces the X-ray and radio morphology.

ZWCL1856 (z=0.304) (Zwicky et al. 1961) (PSZ1 G096.89+24.17) was detected in the Planck SZ Survey and reported to have a mass $M_{500} = 4.7^{+0.3}_{-0.3} \times 10^{14}$ M$_\odot$ (Planck Collaboration et al. 2016). Cross matching WSRT observations with galaxy cluster catalogs, de Gasperin et al. (2014) discovered that ZWCL1856 contains two radio relics. They estimated the northern relic LLS to be 0.9 Mpc in extent and the southern to be 1.4 Mpc. Taking the brightness peak of the smoothed ROSAT X-ray image as the center of the cluster, they found the distance to the northern relic to be 0.77 Mpc and the southern relic to be 1.15 Mpc. The spectral index of the radio emission was not reported because of a lack of radio data.

The symmetry of these two clusters provides the ideal configuration to study the connection between cluster mergers and radio relics. The aim of this study is to enhance our understanding of the merger scenarios that created these double radio relics using multiwavelength observations. Utilizing deep Subaru and *HST* observations of the galaxy clusters, we perform a precision WL analysis of the cluster mass and combine the WL results with X-ray and radio observations to enhance our understanding of the merging process that produced these radio relics.

We outline the observations and data reduction in Section 2. Weak-lensing theory, shape measurement, source selection, and source redshift estimation are in Section 3. Section 4 presents our mass reconstruction and mass estimations for each cluster based on WL and X-ray temperature measurements. We discuss the mass of each substructure and provide evidence for updated merger scenarios in Section 5.

Table 1. Subaru Observations

Filter	EXPTIME (s)	DATE-OBS
MACS1752		
g	750	2013-07-13
r	1470	2013-07-13
i	3630	2013-07-13/2014-02-26
ZWCL1856		
g	750	2015-09-12
r	2190	2015-09-12

Cluster masses are defined as the mass within R_{200} where R_{200} is the radius of a sphere within which the average density is 200 times the critical density of the universe at the cluster redshift. We assume a flat ΛCDM cosmology with $H_0 = 70$ km s^{-1} Mpc^{-1}, $\Omega_\Lambda = 0.7$, and $\Omega_m = 0.3$. For the stated cosmology, the scales are 5.123 kpc arcsec^{-1} and 4.535 kpc arcsec^{-1} for z=0.365 (MACS1752) and z=0.304 (ZWCL1856), respectively.

2. OBSERVATIONS AND DATA REDUCTION

2.1. *Subaru Observations*

We observed MACS1752 and ZWCL1856 with the Subaru Telescope Suprime-Cam on the nights of 2013 July 13, 2014 February 26, and 2015 September 12 (PI: D. Wittman). The multi-band imaging is summarized in Table 1. During observations, a dither and rotation of the camera between shots was applied to enable minimization of stellar diffraction spikes and removal of saturation trails through our data reduction process.

Basic data reduction steps (bias and overscan subtraction, flat fielding, geometric distortion correction, etc.) were performed using the Subaru Suprime-Cam software SDFRED2 (Yagi et al. 2002; Ouchi et al. 2004). We used SCAMP (Bertin 2006) to determine an astrometric solution with Pan-STARRS (Chambers et al. 2016) as the alignment catalog. The astrometric solution was handed to SWARP (Bertin et al. 2002) where a median co-added mosaic image was created. Utilizing the median mosaic image, we masked artifacts such as saturation trails, cosmic rays, bad pixels, etc. and re-SWARPed the images with the mask weighting to produce a mean coadded mosaic image. The mean coadded mosaic images for each galaxy cluster are approximately 40′ in diameter and have the standard 0.″2 pixel scale. We select the observations with the longest exposure times to perform our WL analysis: i-band and r-band for MACS1752 and ZWCL1856, respectively. Figure 1 shows our Subaru imaging for MACS1752 (left) and ZWCL1856 (right) with X-ray (blue) and radio observations (red) of the ICM features enhanced in the RGB image.

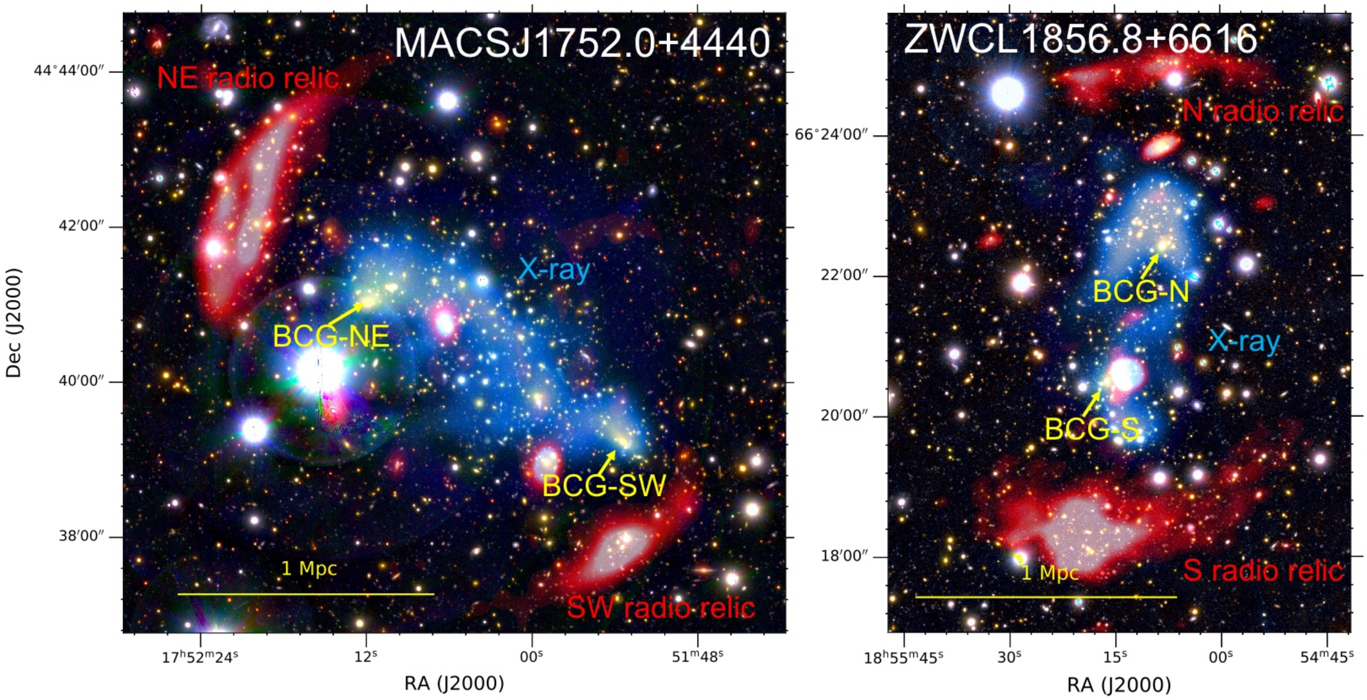

Figure 1. Left: Subaru color image of MACS1752 with 18cm WSRT radio emission (red) from van Weeren et al. (2012) and 0.5-7 keV XMM-*Newton* X-ray emission (blue). Right: Subaru color image of ZWCL1856 with 144 MHz LOFAR radio emission (red) from Jones et al. in prep. and 0.5-7 keV XMM-*Newton* X-ray emission (blue). Arrows mark the locations of the two brightest cluster galaxies (BCGs) for each cluster. The bright X-ray morphology shows an inverted S-shape in both clusters with the BCGs near the ends. The position and alignment of the radio relics in ZWCL1856 are almost mirrored and are located in front of the X-ray brightness peaks. Whereas, the relics appear to be misaligned with the ICM distribution in MACS1752.

2.2. *Hubble Space Telescope Observations*

MACS1752 was observed by the *HST* in three programs 12166 (PI: T. Ebeling), 12844 (PI: T. Ebeling), and 13343 (PI: D. Wittman). Since the angular size of the cluster is much larger than the *HST* field-of-view, two pointings, centered on each brightest cluster galaxy (BCG), were obtained. *HST* observations are summarized in Table 2.

We retrieved FLC images from the Mikulski Archive for Space Telescopes (MAST) archive [2]. These images are delivered already calibrated by the STScI OPUS pipeline. We used `Multidrizzle` (Koekemoer et al. 2003) to perform sky subtraction, geometric distortion correction, and cosmic ray rejection. To accurately align the *HST* frames, common objects were matched between each frame and the offset was iteratively minimized. The alignment shifts were then applied to the images as they were coadded into a mosaic (see Jee et al. 2014, for details). The *HST* imaging provides a deep pointing covering each of the BCG locations (see Figure 1). We select the F814W image for our *HST* shape measurements.

Table 2. HST/ACS Observations

Filter	EXPTIME (s)	DATE-OBS
MACS1752 NE		
F435W	2526	2013-10-26
F606W	2534	2013-10-26
F814W	2394	2013-10-26
MACS1752 SW		
F606W	1200	2011-08-13
F814W	3879	2012-12-07/2014-10-26

2.3. *XMM-Newton Data Reduction*

Both clusters have XMM-*Newton* X-ray observations. MACS1752 was observed on 2010 May 16 (PI: S. Allen; ObsID: 0650383401) for 13 ks and ZWCL1856 was observed on 2013 May 31 (PI: C. Jones; ObsID: 0723160401) for 12 ks. We retrieved the data from the XMM-*Newton* science archive[3] and reduced them using the XMM-*Newton* Extended Source Analysis Software (XMM-ESAS; SAS version 18.0.0). We followed the pro-

---

[2] https://mast.stsci.edu/portal/Mashup/Clients/Mast/Portal.html

[3] http://nxsa.esac.esa.int/nxsa-web/#home

cedures described in the XMM-ESAS Cookbook[4] and conducted standard calibration, filtering, and clearing of flare events. The final MOS1, MOS2, and PN clean exposure times are 12.2, 12.1, and 6.3 ks for MACS1752 and 11.4, 11.1, and 8.9 ks for ZWCL1856. For both clusters, we extracted broad band (0.5-7 keV) images for spectral analysis and soft band (0.5-2 keV) images for imaging analysis. Point sources in the images were detected and removed with the `edetect_chain` task and the remaining holes were filled with the CIAO `dmfilth` task.

2.4. *Point Spread Function Model*

Correction of the distortion caused by the telescope PSF is a critical aspect of a WL analysis. As the waves of light from the distant galaxies pass through the atmosphere and telescope, the wavefronts are deformed causing a broadening of the observed image. This effect must be modeled and removed in order to access the gravitational lensing distortions.

The PSF modeling for *HST* and Subaru follow the same basic principles (see Jee et al. 2007; Finner et al. 2017). The objective is to model the PSF of galaxies that will be used to quantify the WL effect. For Subaru obeservations, our pipeline designs PSF models for the galaxies in the mosaic images by modeling the PSF from stars in each of the component frames of the coadded mosaic and then stacking the component PSFs into a coadded PSF. This technique is required because the PSF across the full mosaic image is too complex to be interpolated and the PSF is discontinuous across CCD gaps. For each of the component frames, unsaturated stars were selected by their size and brightness. A principal component analysis (PCA) of the selected stars was performed and the principle components were used to reconstruct position dependent PSF models for each galaxy on a frame-by-frame basis. Finally, the PSF models from the component frames were stacked into a coadded PSF model.

For *HST* data, the PSF modeling has one major difference in that the images of MACS1752 do not contain enough stars to robustly sample the PSF. Instead, following Jee et al. (2007), we relied on archival *HST* images of globular clusters to model the PSF. This technique works because the PSF of the space-based *HST* repeats on its 1.5 hour orbital period. The PSF models[5] built from the globular cluster images were matched to the MACS1752 images by minimizing the difference between the modeled PSF and the measured shapes of the tens of stars that were found in a single *HST* MACS1752 pointing. Once the best-fit model for each frame was found, the PSF for the galaxies was modeled and coadded, as was done with Subaru.

In Figure 2, we show the ellipticity of stars from the Subaru mosaic images. Red circles mark the star ellipticity components before PSF correction and black circles mark them post correction. As desired, the corrected ellipticities are more circular and centered close to (0,0). The mean values of the corrected ellipticities of stars are $\langle e_1 \rangle = 5e\text{-}4$ and $\langle e_2 \rangle = 1e\text{-}4$ for MACS1752 and $\langle e_1 \rangle = 5e\text{-}4$ and $\langle e_2 \rangle = 1e\text{-}3$ for ZWCL1856.

3. WEAK-LENSING METHOD

3.1. *Theory*

The gravitational potential of a galaxy cluster causes a deflection of the light coming from more distant galaxies. This is observed as a distortion of the shapes of galaxies as described by the following linear transformation matrix:

$$A = \begin{pmatrix} 1-\kappa-\gamma_1 & -\gamma_2 \\ -\gamma_2 & 1-\kappa+\gamma_1 \end{pmatrix}, \tag{1}$$

which is dependent on κ, the convergence, and γ, the shear. The convergence is an isotropic distortion that is a function of the projected mass density Σ and the critical surface density Σ_c:

$$\kappa = \frac{\Sigma}{\Sigma_c}. \tag{2}$$

The critical surface density,

$$\Sigma_c = \frac{c^2 D_s}{4\pi G D_l D_{ls}}, \tag{3}$$

is a function of the speed of light c, the gravitational constant G, and varies with angular diameter distance to the cluster (lens) D_l and with the ratio of angular diameter distances from lens to source and from observer to source D_{ls}/D_s. The ratio $\beta = D_{ls}/D_s$ is often referred to as the lensing efficiency. The shear γ encodes the anisotropic distortion and can be conveniently described as a complex shear $\gamma = \gamma_1 + i\gamma_2$. Positive and negative values of γ_1 describe distortions along the x and y axes, respectively. Whereas, positive and negative values of γ_2 describe distortions along the $y = x$ and $y = -x$ directions, respectively. In reality, we observe the combined effects of γ and κ, which we refer to as the reduced shear $g_i = \gamma_i/(1-\kappa)$.

3.2. *Shape Measurement*

---

[4] http://heasarc.gsfc.nasa.gov/docs/xmm/esas/cookbook/

[5] http://narnia.yonsei.ac.kr/∼mkjee/acs_psf/

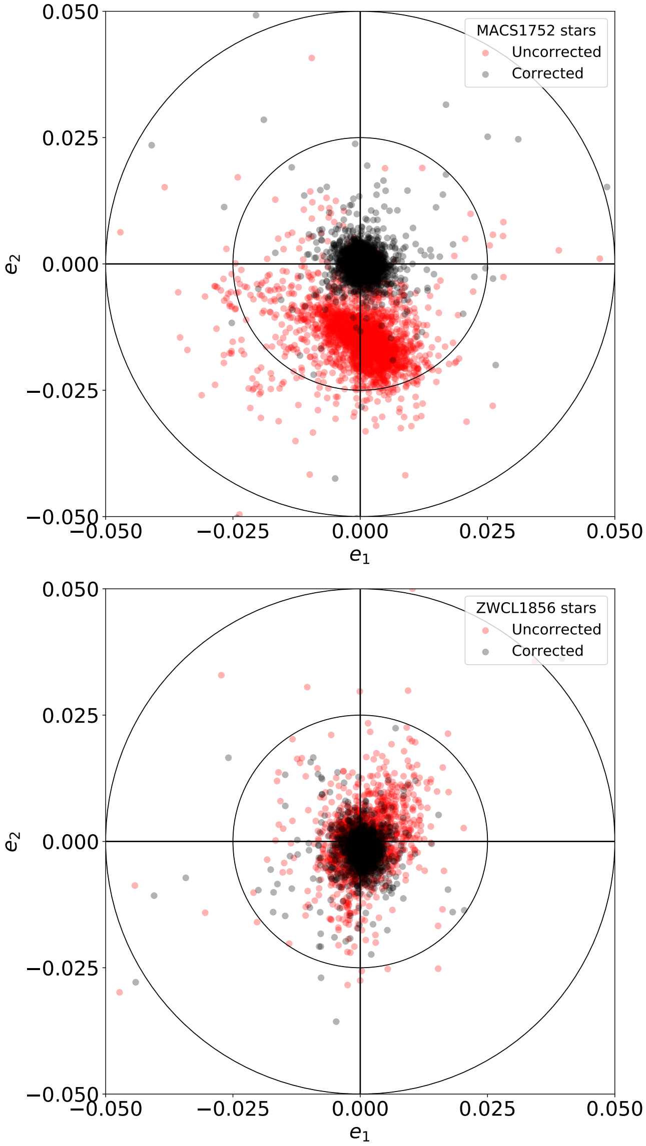

Figure 2. Subaru ellipticity corrections for MACS1752 (top) and ZWCL1856 (bottom). Red circles denote the uncorrected ellipticities of stars from the mosaic image. Black circles are the corrected ellipticities after subtracting the shape of the PSF model for each star. The distributions both tighten and shift towards (0,0).

Detection of the WL effect requires a statistical analysis of the shapes of distorted galaxy images. We employed a model-fitting technique to measure the shapes of galaxies. The shape measurement was performed on the *HST* F814W and Subaru *i*-band imaging for MACS1752 and Subaru *r*-band for ZWCL1856. The procedure for each filter was identical.

To measure the shape of a single galaxy, we cut out a postage stamp image of the galaxy from the mosaic image. A corresponding rms noise postage stamp $\sigma_{\rm rms}$ was also cut out from the rms mosaic image. It is important to consider the size of the postage stamp image. A large postage stamp image will contain the light from nearby objects, which may significantly alter the shape measurement. However, a small postage stamp may prematurely truncate the galaxy light profile and lead to truncation bias (see Mandelbaum et al. (2015) for more on truncation bias). We chose to cut large postage stamp images that are eight times the size of the half-light radius as measured by `SExtractor` (Bertin & Arnouts 1996), with a 10 pixel floor for very small objects. Making use of the `SExtractor` segmentation map, we masked any nearby bright objects that could influence the shape measurement by setting the relevant pixels in the rms noise postage stamp to 10^6.

We fit an elliptical Gaussian function, G, to the postage stamp image, I, while forward-modeling the corresponding PSF model, P, as follows:

$$\chi^2 = \sum \left(\frac{I - G \circledast P}{\sigma_{\rm rms}} \right)^2 , \tag{4}$$

where the summation is over the pixels of the postage stamp. The elliptical Gaussian function has seven free parameters: background, amplitude, position (x and y), semi-major axis (a), semi-minor axis (b), and orientation angle (ϕ). We fixed the background, x, and y while fitting the remaining four parameters. Complex ellipticities were determined from a, b, and ϕ as

$$e_1 = \frac{a-b}{a+b} \cos 2\phi, \tag{5}$$

$$e_2 = \frac{a-b}{a+b} \sin 2\phi. \tag{6}$$

This procedure was repeated for each galaxy in each filter and filter-dependent shape catalogs were compiled. It is known that galaxy shape measurement techniques suffer from bias (for more on WL biases see Mandelbaum 2018). We derived a calibration factor from simulations of our pipeline to correct for multiplicative bias. The multiplicative calibration factors are 1.15 (1.25) for Subaru (*HST*) ellipticities. These calibrations were derived through pipeline tests on simulated images (Jee et al. 2013). At this point, the catalog contains stars as well as foreground, cluster, and background galaxies. In the following section, the shape catalogs will be refined to a source catalog containing the lensed background galaxies.

3.3. *Source Selection*

The ideal catalog for a WL analysis contains only galaxies that are at a greater distance than the lens (cluster) from the observer. Direct distance measurements for each object would make source selection trivial. As one can imagine, gathering spectroscopic redshifts for of order 20,000 galaxies is an immense undertaking. Photometric redshifts rely on multiband imaging, which is often not available for specific galaxy clusters. With redshifts unavailable, we instead rely on the color and magnitude of galaxies to categorize them. The rest-frame 4000Å break, a prominent feature in the spectral energy distribution (SED) of evolved cluster galaxies, forms a red-sequence relation in color when observed with two filters that bracket the feature. At the redshift of ZWCL1856 (0.304) and MACS1752 (0.365), the 4000Å breaks are at wavelengths of 5216Å and 5460Å, respectively. The feature is well bracketed by the g and r or g and i filters.

For MACS1752, we modeled shapes in *HST* and Subaru imaging. Figure 3 is the color-magnitude diagram for MACS1752 Subaru imaging (top) and *HST* imaging (bottom). The red circles represent galaxies with spectroscopic redshifts from the catalog of Golovich et al. (2019b) within $\Delta z = 0.03$ of the BCG redshift. We set the criteria for background galaxies to be those that are bluer than the red sequence and fainter than 23rd magnitude. Furthermore, we required the semi-minor axis of objects to be $b > 0.3$ pixels to remove objects that are too small to be lensed galaxies, the magnitude uncertainty to be $dm < 0.3$, and the measured ellipticity $e < 0.9$ and its uncertainty $de < 0.3$ to prevent poorly fit objects from entering the source catalog. This source selection provides ~26 galaxies arcmin^{-2} (~83 galaxies arcmin^{-2}) for MACS1752 Subaru (*HST*) imaging.

Source galaxies in ZWCL1856 were selected using the same constraints as for the Subaru imaging of MACS1752, except that the magnitude cut was set to the 22nd magnitude to take advantage of the lower redshift of the cluster. The source density is ~31 galaxies arcmin^{-2} for ZWCL1856 Subaru imaging.

3.4. *Source Redshift Estimation*

In a WL analysis, each source galaxy provides a probe of the projected galaxy cluster potential. As is apparent in Equation 3, the effectiveness of the gravitational lens varies on a source-by-source basis with the lensing efficiency ratio, β. As mentioned, distances to each of the source galaxies in our sample are unavailable. To remedy this, we rely on the photometric redshift catalog (Dahlen et al. 2010) of the GOODS-S field as a reference for our source galaxy catalog. This technique is common in WL studies that do not have the luxury of redshifts for each source galaxy (to name a few, Jee et al. 2011; Okabe & Smith 2016; Schrabback et al. 2018).

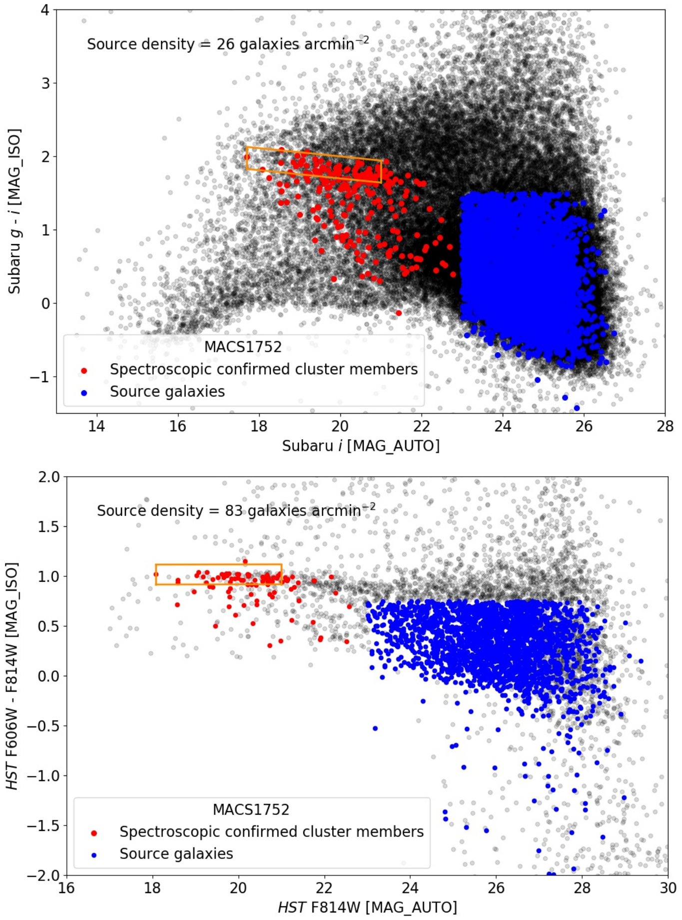

Figure 3. MACS1752 color-magnitude diagrams for Subaru (top) and *HST* (bottom). Red circles represent spectroscopically confirmed cluster members within redshift of 0.03 of the BCG. A tight red sequence relation is found in the *HST* CMD. Extending the range of spectroscopic cluster members to the Subaru field of view shows that there are many bluer members. By a linear fit to the reddest spectroscopic member galaxies (the red sequence), galaxies within $(g - i) \pm 0.1$ in Subaru or $(F606W - F814W) \pm 0.1$ in *HST* were selected as photometric red-sequence candidates (orange parallelograms). Blue circles are the galaxies selected for the background source catalog based on their relation to the red sequence and the shape criteria mentioned in the Section 3.3. The dense feature found underneath the red sequence in the Subaru CMD arises from Galactic stars and shows a trend of brighter and bluer.

For our three source catalogs, we derived a GOODS-S reference catalog by applying the same magnitude and color constraints as was applied during source selection (Section 3.3). Photometric transformations were applied when necessary to convert the *HST* filters to match the Subaru filters. Then, the galaxy number density as a function of magnitude for each source catalog was compared to the corresponding constrained GOODS-S reference catalog. The difference in depth was corrected

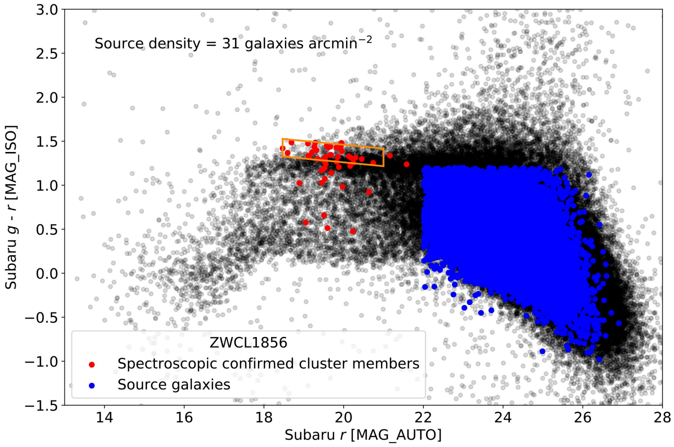

Figure 4. Subaru color-magnitude diagram for ZWCL1856. Red circles are spectroscopically confirmed cluster members. Orange parallelogram is the photometric red-sequence candidate selection. Blue circles represent galaxies selected for the background source catalog. The dense feature found underneath the red sequence arises from Galactic stars and shows a trend of brighter and bluer.

by weighting the constrained GOODS-S reference catalog to match the number density of each source catalog. Finally, the three constrained and weighted GOODS-S photometric redshift distributions were used to estimate the lensing efficiency and corresponding effective redshift of the galaxies in our source catalogs. We restrict the lensing efficiency to

$$\beta = \left\langle max\left(0, \frac{D_{ls}}{D_s}\right)\right\rangle, \tag{7}$$

which forces foreground galaxies to have $\beta = 0$. The lensing efficiency of Subaru source galaxies for MACS1752 is $\langle\beta\rangle = 0.53$ (effective redshift $z_{\text{eff}} = 0.89$) with a width of the distribution of $\left\langle\beta^2\right\rangle = 0.33$ and for *HST* $\langle\beta\rangle = 0.62$, $z_{\text{eff}} = 1.18$, and $\left\langle\beta^2\right\rangle = 0.41$. The lensing efficiency for ZWCL1856 is $\langle\beta\rangle = 0.54$ with $z_{\text{eff}} = 0.76$ and width of the distribution of $\left\langle\beta^2\right\rangle = 0.36$.

The bias caused by approximating the source distance and distribution of the source population by a single characteristic value has been discussed in detail in Seitz & Schneider (1997) and Hoekstra et al. (2000). In our analysis, the width of the distribution is accounted for by modifying the reduced shear g to the corrected reduced shear:

$$g' = \left[1 + \left(\frac{\left\langle\beta^2\right\rangle}{\left\langle\beta\right\rangle^2} - 1\right)\kappa\right] g, \tag{8}$$

where κ is the convergence as defined in Section 3.1.

4. RESULTS

4.1. *Mass Reconstruction*

The Subaru observations have a footprint that extends approximately 40 arcmins in diameter. This footprint covers 3 ∼ 4 virial radii at the redshifts of ZWCL1856 (z=0.304) and MACS1752 (z=0.365). We used the FIATMAP code (Fischer & Tyson 1997) to convert galaxy ellipticities to a convergence map, which performs a real-space convolution.

The mass distribution of MACS1752 is shown in the left panel of Figure 5. Two dominant mass peaks are detected at opposite ends of the mass distribution that have excellent agreement with the NE and SW BCGs. In addition, a substructure is detected between the primary clusters, ~443 kpc northeast of the SW BCG. This mass substructure has a bright cluster galaxy companion. To test the significance of the peaks, we performed bootstrap resampling to create 1000 realizations of the source catalog and mass map. The resulting 1σ distributions of the mass peaks are marked as the violet dashed contours in the left panel of Figure 5. The signal-to-noise (S/N) convergence contours derived from bootstrapping are labeled in Figure 5 and the peak S/N values are summarized in Table 3. The NE mass peak has the strongest detection at the 7.9σ level, followed by the SW mass peak at 6.5σ and finally the central peak at 5.5σ.

Next, we compare the mass distribution to the cluster galaxy distribution. A spectroscopic analysis of MACS1752 (Golovich et al. 2019a) identified 176 cluster galaxies. To supplement the spectroscopic members, we photometrically determined cluster galaxies from the CMD in Figure 3 by selecting those with Subaru $(g-i)\pm0.1$ or *HST* $(F606W - F814W)\pm0.1$ along a linear fit to the red sequence. This selection is highlighted by the orange parallelogram in Figure 3. The cluster galaxy luminosity and number density distributions are shown in the right panels of Figure 5. In the top panel, the S/N contours trace the luminosity distribution of the cluster galaxies. As expected, the brighter peaks coincide with the S/N peaks. The number density distribution of galaxies in the bottom panel again shows good spatial agreement with the S/N contours.

Like MACS1752, the mass map of ZWCL1856 (Figure 6) shows two dominant peaks. From bootstrapping, the peak significances are S/N=4σ in the north and S/N=3.7σ in the south and both show excellent agreement with the corresponding BCG locations. An elongation from the southern mass peak to the center is detected that is similar to that in MACS1752 and, although there are some cluster galaxies in the region, no clear sign of a BCG is visible. The galaxy luminosity distribution (top right panel) reveals that the southern peak is 1.5 times brighter than the northern, which is in contrast to the lensing S/N that is 1.1 times higher for the northern peak. However, the number density distribution (bottom right panel) shows a more equal weight to each subcluster.

4.2. *Mass Estimation*

The lensing signal that is detected around merging galaxy clusters arises from the entire mass distribution. Therefore, to properly determine the mass from the lensing signal, the contribution of each structure to the observed shear should be carefully modeled. Our convergence maps reveal that MACS1752 is composed of three significant subclusters and ZWCL1856 is composed of two. In this section, we derive the masses of these subclusters.

We estimated the mass of each subcluster by superposing NFW halos (Navarro et al. 1997) and modeling the expected tangential shear at each source galaxy position. We fixed the centroid of each subcluster halo to its respective BCG. Due to recent merging activity, the BCG may not necessarily coincide with the mass peak. However, for the two clusters that are presented in this work, the mass peaks and their corresponding BCGs are in good agreement. Nevertheless, the core regions (∼200 kpc) around each subcluster were removed to bypass the effects of the strong lensing regime and the region where additional systematic effects can lead to a biased mass estimate. We elected to not use a concentration-mass (c-M) relation to estimate the mass of each subcluster because most c-M models are valid only within the cosmology and mass range of the simulations from which they are derived. Instead, we sampled the posterior distribution of the mass and concentration with Markov Chain Monte Carlo (MCMC). Priors were set on the concentration and mass of $1 < c < 6$ and 10^{13} M$_\odot$ $< M_{200} < 10^{16}$ M$_\odot$. These priors amply cover the typical range of galaxy cluster masses and concentrations that arise in numerical simulations (e.g. Duffy et al. 2008; Diemer & Joyce 2019). The mass estimates from MCMC are summarized in Table 3 and reveal that both MACS1752 and ZWCL1856 are approximately 1:1 mass ratio mergers. Concentrations are unconstrained by this method. Since the central subcluster in MACS1752 is low mass ($0.3^{+0.4}_{-0.1} \times 10^{14}M_\odot$), we will exclude it from our examination of the merger.

The total M_{200} of each system is not simply the addition of the subcluster masses but is the mass within a radius at which the combined average density of the subclusters is 200 times the critical density of the universe at the cluster redshift. To calculate the total mass, two NFW halo models were stacked in a 3D grid with locations given by their measured projected separation. Integrating radially from the midpoint, the total mass was calculated. This procedure was repeated for each sample from the MCMC chains to sample the total mass distribution without using a c-M relation. The total mass of MACS1752 is $M_{200} = 14.7^{+3.8}_{-3.3} \times 10^{14}$ M$_\odot$ and the total mass of ZWCL1856 is $M_{200} = 2.4^{+0.9}_{-0.7} \times 10^{14}$ M$_\odot$.

4.3. *M/L Ratio*

The mass-to-light ratio (M/L) of galaxy clusters has been used as a probe of cosmology to measure the matter density of the universe. Carlberg et al. (1996) examined 16 X-ray luminous galaxy clusters and determined the M/L ratio of clusters is ∼300 M$_\odot$/L$_\odot$ by using the velocity dispersion of cluster galaxies. Girardi et al. (2002) showed that the M/L ratio of galaxy clusters is positively correlated with cluster mass and has a large scatter that ranges from 50 ∼ 1000 M$_\odot$/L$_\odot$.

We measured the M/L ratio for each subcluster of MACS1752 and ZWCL1856. Centered on the respective BCG, equal-sized apertures were placed that maximize the size without overlap (MACS1752 radius=550 kpc, ZWCL1856 radius=300 kpc). These apertures were used to evaluate the projected mass and galaxy luminosity within. The projected mass was calculated by integrating the projected density of an NFW halo (Wright & Brainerd 2000) that was modeled with our WL mass and concentration samples from MCMC. To derive the total luminosity within the aperture, we used our cluster galaxy catalogs (compiled in Section 4.1) that include the spectroscopically confirmed cluster members and the photometrically selected sample. For easier comparison with literature, i- (MACS1752) and r-band (ZWCL1856) magnitudes were converted to absolute magnitudes and then transformed to Johnson B-band absolute magnitudes by synthetic photometry (Sirianni et al. 2005) with SED templates for elliptical, spiral, and irregular galaxies. Lastly, solar luminosities were calculated from the magnitudes by assuming $B_\odot = 5.48$. The M/L ratios are presented in Table 3. The M/L ratios found are within the range that is predicted from Girardi et al. (2002). Furthermore, the M/L ratios follow the expected trend with more massive clusters having larger ratios.

4.4. *X-ray analysis*

X-ray analysis plays an important role in interpreting merging scenarios, especially in radio relic clusters. To our knowledge, no in-depth analysis of the archival X-ray data on these specific clusters has been published.

To measure average global temperatures of the systems, we extracted spectra from the point source masked

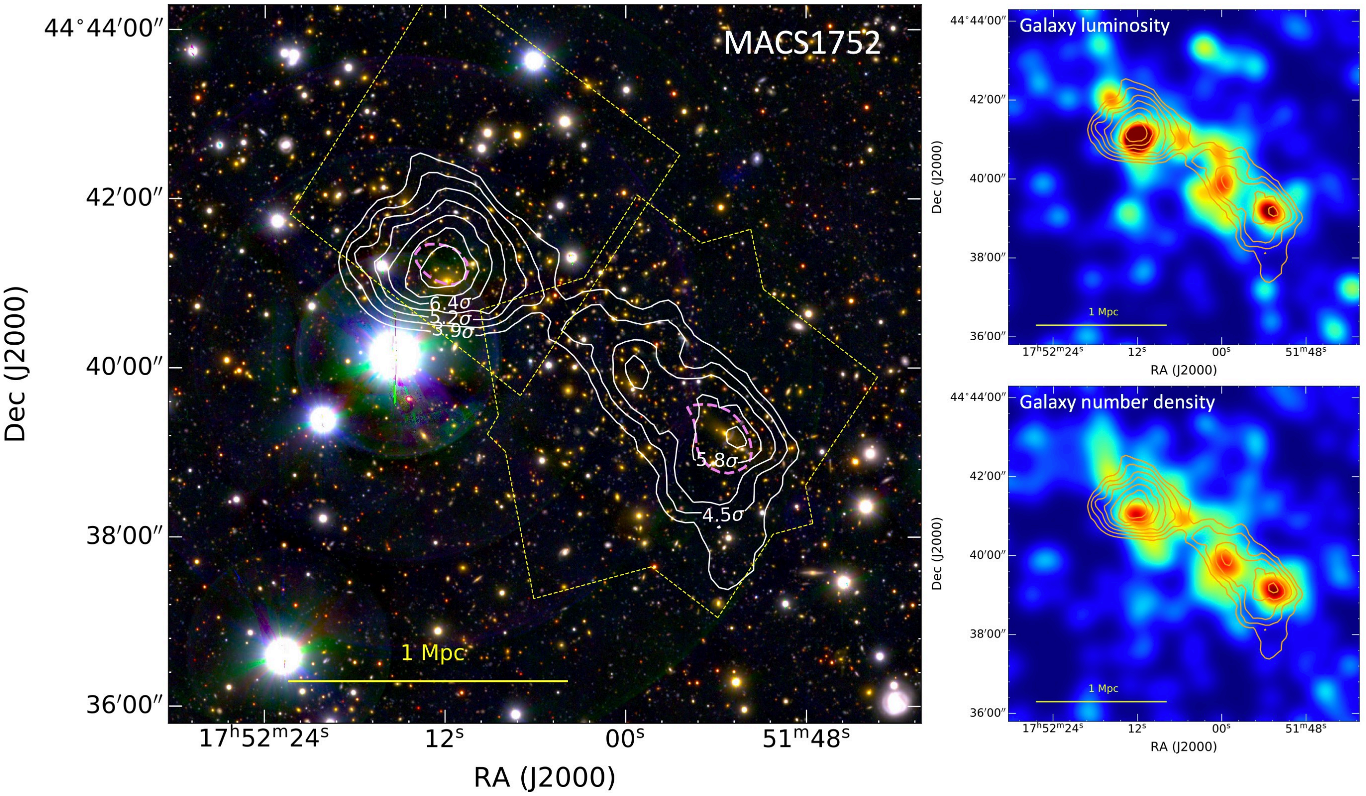

Figure 5. Left: Fiatmap reconstruction of the mass distribution of MACS1752 derived from *HST* and Subaru shapes plotted over Subaru color image. Contours are labeled with S/N values derived from bootstrapping. The dashed violet contours show the 1σ peak uncertainty from bootstrapping. The mass peaks are in statistical agreement with the respective BCG. The dashed yellow line outlines the *HST* footprint. Top-right: Convergence contours (orange) over cluster galaxy *i*-band luminosity colormap. Bottom-right: Convergence contours (orange) over cluster galaxy number density colormap. Galaxy distributions are smoothed with a $\sigma = 18''$ Gaussian kernel.

Table 3. Measured Properties of MACS1752 and ZWCL1856

Subcluster	RA	Dec.	BCG redshift	M_{200} $10^{14}\mathrm{M}_\odot$	Peak S/N	M/L $\mathrm{M}_\odot\ \mathrm{L}_\odot^{-1}$	σ_v km s^{-1}	T keV
MACS1752				[a]		[b]		
NE	$17^{\mathrm{h}}51^{\mathrm{m}}53^{\mathrm{s}}.4$	$44°39'14''$	0.3648	$5.6^{+1.8}_{-1.6}$	7.9	498^{+102}_{-100}	1006 ± 60	$7.6^{+2.4}_{-1.5}$
SW	$17^{\mathrm{h}}52^{\mathrm{m}}11^{\mathrm{s}}.9$	$44°41'02''$	0.3634	$5.6^{+1.4}_{-2.1}$	6.5	412^{+91}_{-93}	1038 ± 77	$6.8^{+3.4}_{-1.7}$
Center	$17^{\mathrm{h}}51^{\mathrm{m}}59^{\mathrm{s}}.6$	$44°39'49''$	0.3617	$0.3^{+0.4}_{-0.1}$	5.5			
ZWCL1856								
N	$18^{\mathrm{h}}56^{\mathrm{m}}33^{\mathrm{s}}.6$	$66°23'57''$	0.3041	$1.2^{+0.5}_{-0.5}$	4.0	360^{+102}_{-106}	934 ± 117	$4.3^{+2.1}_{-1.1}$
S	$18^{\mathrm{h}}56^{\mathrm{m}}41^{\mathrm{s}}.5$	$66°21'56''$	0.3033	$1.0^{+0.4}_{-0.7}$	3.7	183^{+84}_{-97}	862 ± 133	Unconstrained

[a] Combined Subaru and *HST* sources boost S/N for MACS1752

[b] Velocity dispersion (σ_v) measurements from Golovich et al. (2019a)

MOS1, MOS2, and PN images within a circular region ~6′ in diameter (yellow dashed circles in Figures 7 and 8). The combined MOS and PN spectra were analyzed using `XSPEC` (`v12.10.1f`) with the `APEC` plasma model and the `PHABS` photoelectric absorption model in the broad energy band (0.5-5 keV). We assumed a fixed abundance of 0.3 $Z_\odot$ and fixed neutral hydrogen column densities of 3.2×10^{20} cm^{-2} and 9.9×10^{20} cm^{-2} for MACS1752 and ZWCL1856, respectively (HI4PI Collaboration et al. 2016). We find the global temperatures of MACSJ1752 and ZWCL1856 to be $kT = 5.9^{+1.0}_{-0.9}$ keV and $kT = 3.7^{+0.6}_{-0.5}$ keV. The same method was used to determine temperatures for each subcluster within the apertures used for M/L determination. These temper-

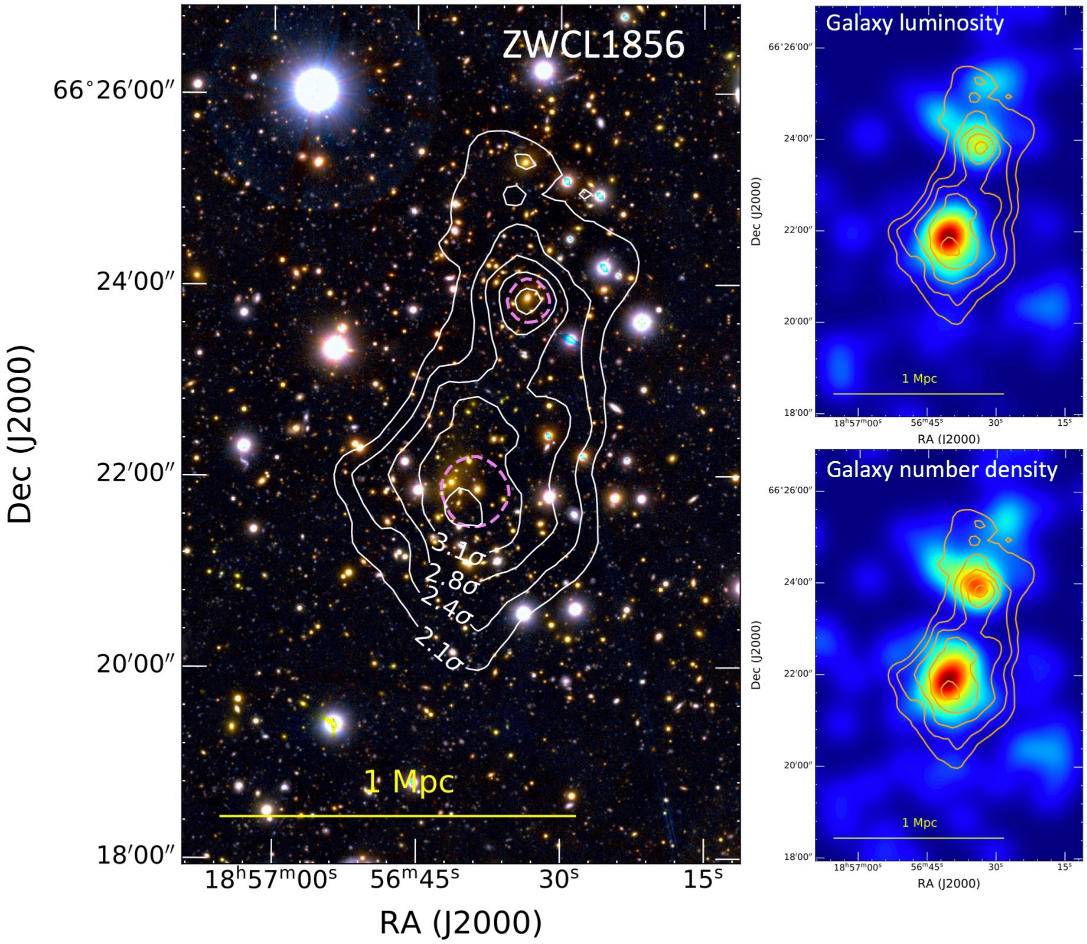

Figure 6. Fiatmap reconstruction of the mass distribution of ZWCL1856 with Subaru color image in background. The dashed violet contours show the 1σ peak uncertainty from bootstrapping. Top-right: Convergence contours (orange) plotted over the cluster member galaxy r-band luminosity. Bottom-right: Convergence contours (orange) over galaxy number density. Galaxy distributions are smoothed with a $\sigma = 18''$ Gaussian kernel.

atures are presented in Table 3. The temperature of ZWCL1856 S was unable to be constrained due to low source counts.

As radio relics are expected to arise at merger shocks, we attempted to detect the shock in the X-ray emission from the ICM. Using the radio relic locations as a guide, we extracted the X-ray surface brightness profile from the soft-band (0.5-2 keV) background-subtracted, exposure-corrected, point-source-subtracted images in fan-shaped regions marked with green lines in Figures 7 and 8. The extracted profiles were rebinned to have a minimum S/N > 5. Using `PROFFIT v1.5` (Eckert et al. 2011), we first attempted to fit a broken power law to the extracted surface brightness profile and if that failed we fit a single power law. The right panels of Figure 7 show a surface brightness drop between the leading edge of both MACS1752 subclusters and their respective radio relic with compression factors of $C = 1.5 \pm 0.2$ and 2.6 ± 0.3 for the NE and SW subclusters, respectively. We interpret these surface brightness drops as indicators of cold fronts (contact discontinuities) because they do not coincide with the radio relics.

We performed the same analysis for ZWCL1856 and found that a single power-law fit best with no visible drop (Figure 8). In addition, we attempted to determine the temperature of the region outside the radio relics for both clusters but a robust detection was not possible.

5. DISCUSSION

5.1. *Identification of the Substructures*

The observational identification of subclusters is a difficult task. The ultimate goal would be to reconstruct the merger by properly accounting for all subclusters. However, observations are all projected quantities and are limited by their sensitivity and noise. In our study, we have identified subclusters as those that have WL S/N $> 3\sigma$ and coincident galaxy peaks. Although we did not include the ICM features as a criteria for sub-

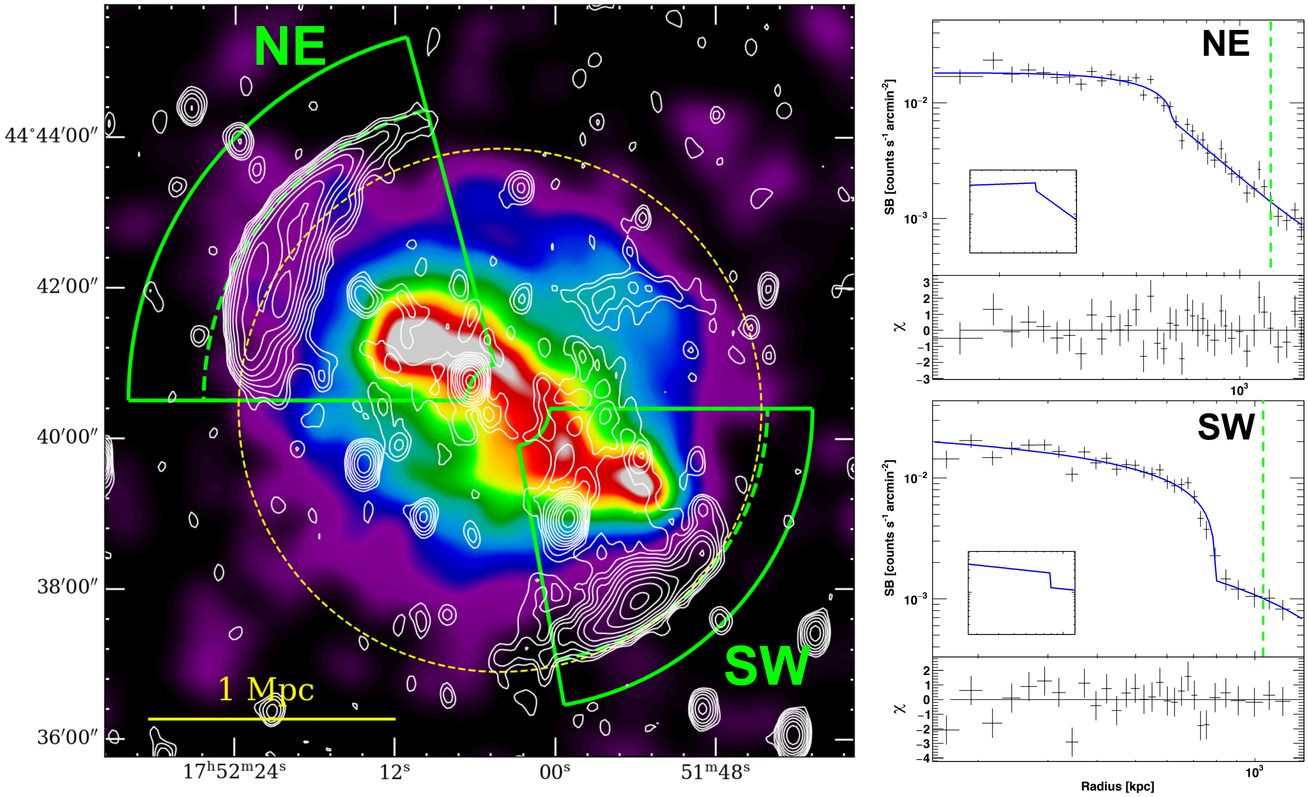

Figure 7. Left: Adaptively smoothed, background-subtracted, exposure-corrected XMM-*Newton* image for MACS1752. Green fan-shaped regions correspond to the areas for the X-ray surface brightness analysis shown in right panels. Yellow dashed circle indicates the region used to extract the global X-ray temperature. Top right: X-ray surface brightness profile (black cross) with a line of sight projected and XMM-*Newton* PSF convolved broken power-law fit (blue solid line) for the northeast core. The edge of the relic is indicated by the green dashed line. Inset image shows the 3D gas density model. Bottom right: Same as the upper panel, but for the southwest core.

structure identification, the substructures also tend to agree with the underlying ICM distribution as revealed by the XMM-*Newton* observations.

The global distributions of WL mass, gas, and galaxies in MACS1752 follow a similar morphology. As revealed by the WL mass reconstruction, MACS1752 is predominantly composed of two subclusters (NE and SW) that are co-spatial with the BCGs and the X-ray brightness peaks. The elongated distribution of the bright X-ray emission from the ICM follows an inverted S shape that terminates at the subclusters. From the NE subcluster, an ICM tail appears to have been stripped from the subcluster (left panel of Figure 9). This ram-pressure stripped gas extends from the NE subcluster about 0.5 Mpc in the cluster center direction. An X-ray tail of this extent would require a powerful ram-pressure force and is suggestive of a low impact parameter for the collision. From the SW subcluster, an extension of the gas towards the center of the cluster may also be caused by ram pressure. However, this extension also coincides with the less significant central WL mass detection and X-ray peak. It is difficult to say whether the central substructure is involved in the merger or is a foreground substructure that will merge later. The BCG that coincides with the mass peak is at $z = 0.3617$, which is slightly lower redshift than the SW and NE BCGs (Table 4). Higher resolution or S/N X-ray observations may provide insight into the nature of this third substructure.

The WL signal of ZWCL1856 is dominated by the N and S subclusters. Based on our bootstrap analysis, the mass peaks in the N and S are consistent with the corresponding X-ray brightness peaks. The resemblance of the WL mass and X-ray emission distributions of ZWCL1856 to MACS1752 is extraordinary. An extension of the WL mass distribution to the north of the S subcluster is apparent. This is comparable to the extension seen from the SW subcluster in MACS1752 but remains unidentified because of the lack of cluster galaxies in the region. The X-ray emission also shows evidence of stripping with a connection between the subclusters that resembles the inverted S shape of MACS1752.

5.2. *Merger Scenarios*

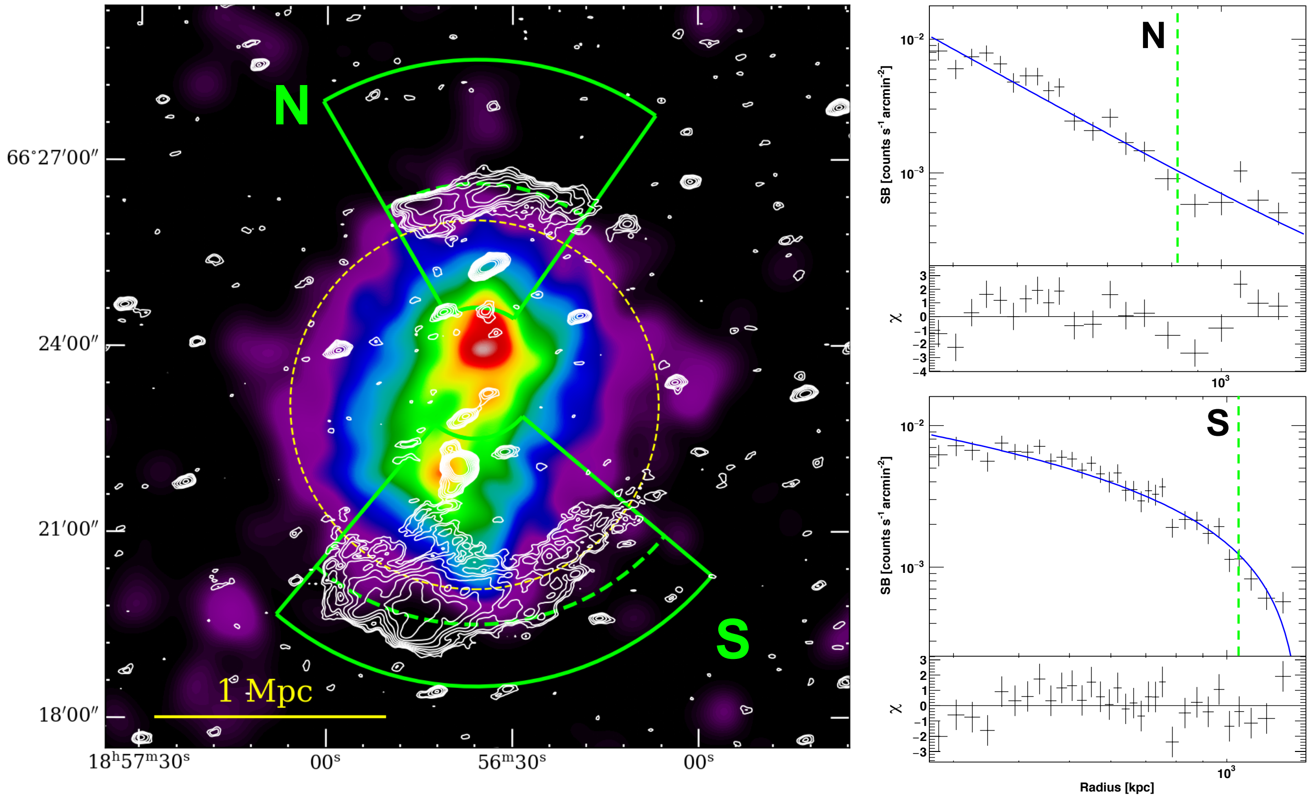

Figure 8. Left: Adaptively smoothed, background-subtracted, exposure-corrected XMM-*Newton* image for ZWCL1856. Green fan-shaped regions correspond to the areas for the X-ray surface brightness analysis shown in right panels. Yellow dashed circle indicates the region used to extract the X-ray temperature. Top right: X-ray surface brightness profile (black cross) with a line of sight projected and XMM-*Newton* PSF convolved power-law fit (blue solid line) for the northern core. The edge of the relic is indicated by the green dashed line. Bottom right: Same as the upper panel, but for the southern core.

Gathering the radio information from the literature and combining it with our new WL mass maps, mass estimates, and X-ray analysis, we revisit the merging scenarios for two of the most symmetric double radio relic clusters. The merger parameters that are of particular interest to reconstructing the past merger are the separation of the subclusters, the collision velocity and direction, the observed phase, and the time since collision.

5.2.1. *MACS1752*

The multiwavelength view of MACS1752, shown in the left panel of Figure 9, presents a binary merger between the NE and SW subclusters. Our lensing analysis found that this is a 1:1 mass ratio merger. This mass ratio is in agreement with galaxy velocity dispersion measurements from Golovich et al. (2019a) (Table 3). On the other hand, from the brightness of the radio relics van Weeren et al. (2012) proposed a 2:1 mass ratio merger and in the simulation of Bonafede et al. (2012) a 3:1 mass ratio merger was suggested.

The path that the merger unfolded along may be inferred from the distribution of the X-ray emission. The X-ray tail that lags behind the NE subcluster is a good indicator of the path that the NE subcluster followed. Given the equality of the subcluster masses, we expect the SW subcluster to have followed a similarly shaped path in the opposite direction. A poorly defined ram-pressure stripped tail extends from the SW subcluster and eventually blends in with the central substructure. The schematic view of the merger is shown in the right panel of Figure 9.

We simplify the merger scenario by defining a collision axis. With the absence of a consensus on the definition of a collision axis from literature, we propose that the collision axis should be defined from the antiparallel velocity vectors that connect the dark matter at pericenter. However, we cannot directly observe the subcluster motions and must find a collision axis proxy. One method is to utilize the positions and orientations of the radio relics as a proxy. In some double radio relic clusters (e.g. CIZA J2242.8+5301, ZWCL 0008.8+5215) connecting the centers of the radio relics with a line gives an approximation of the collision axis that is not very different than the expected axis at pericenter. This is

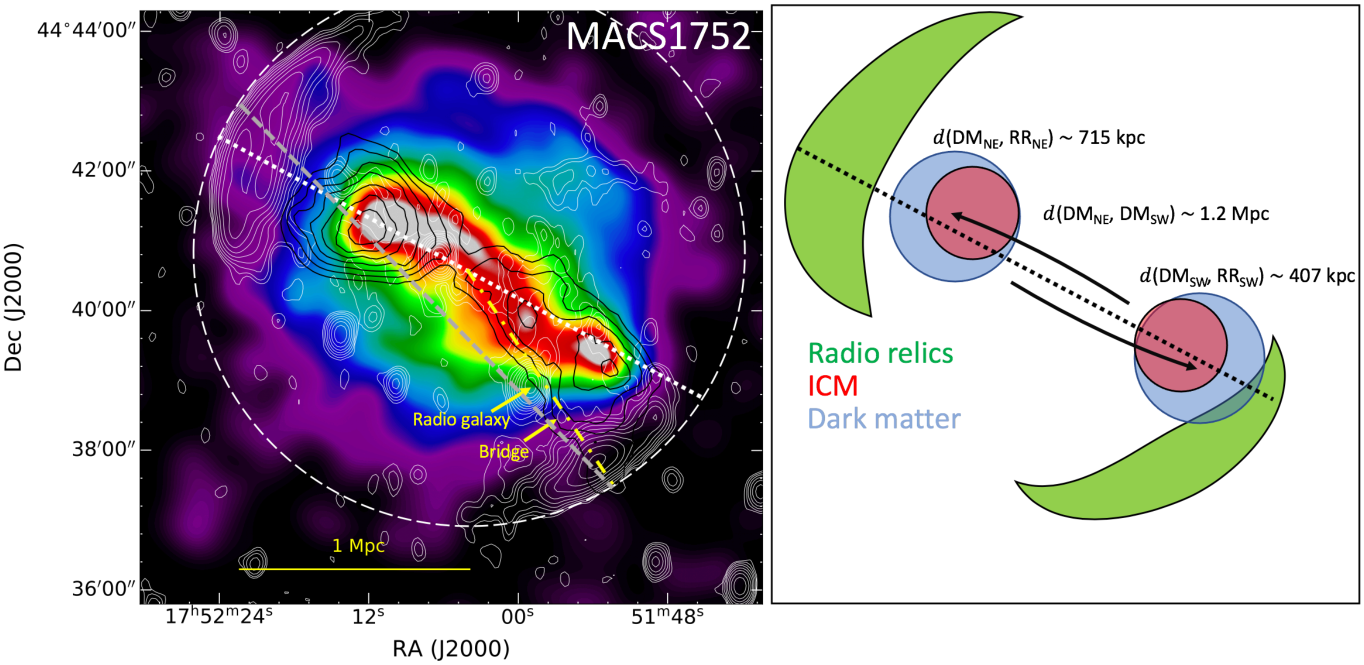

Figure 9. Left: XMM-*Newton* X-ray emission (0.5-7 keV) with WSRT 18 cm radio emission contours in white and WL mass contours in black. The white dotted line is the proposed merger axis. The grey dotted line is the axis connecting the centers of the radio relics. The agreement between the mass peaks and X-ray emission peaks is clear. The NE radio relic appears to be aligned with the merger axis but the SW radio relic is pointed (yellow dash-dot branch) ~25 degrees clockwise from the merger axis. We theorize that this is due to re-acceleration of non-thermal electrons from the radio galaxy that lies between the barycenter of the cluster and the center of the radio relic. A bridge of radio emission extends from the radio galaxy to the radio relic. Right: Schematic of the merger scenario with measured distances. A merger with a non-zero impact parameter between two equal mass subclusters is depicted.

also demonstrated for shocks in the simulations of Ricker & Sarazin (2001) and ZuHone (2011) but may not necessarily be true for radio relics if they depend on the local ICM properties. For MACS1752, reconciling the radio relic defined collision axis (grey dotted line in left panel of Figure 9) with the X-ray morphology and the observed locations of the WL peaks is difficult. Instead, we suggest that the collision occurred offset from the radio relic defined collision axis. As an alternative, we take the major axis of an elliptical Gaussian fit to the X-ray emission as the collision axis. This new collision axis (heavier white dotted line in Figure 9) bisects the WL and X-ray peaks and is ~25 degrees rotated counterclockwise from the relic defined collision axis. For robustness, we also tested elliptical Gaussian fits to the galaxy and WL distributions and found them to indicate a similar collision axis. More detail on the relation of the radio relics and the merger is presented in the upcoming Section 5.4.

Recreating radio relics in numerical simulations is often done by modeling the kinetic energy flux, which is proportional to the collision velocity of the subclusters. We tested three methods to approximate the collision velocity of MACS1752:

- We ran MCMAC (Dawson 2013) with the parameters given in Table 4. MCMAC samples the posterior distribution of a binary head-on collision of NFW halos. We supplied our mass estimates and subcluster separation as input parameters and constrained the merger to be within 30 degrees of the sky (Golovich et al. 2019a; Wittman 2019). The top panel of Figure 11 displays the 3D velocity (v_{3d}) and time since collision (TSC) of MCMAC for 200000 samples. We note that the velocity (TSC) found from MCMAC is expected to be biased lower (higher) than the true collision velocity (TSC) because the halos are released from their current separation and given an initial relative velocity between zero and the free-fall velocity. MCMAC found the time since TSC to be $0.89^{+0.16}_{-0.25}$ Gyrs. Wittman (2019) explained that the head-on collision assumption in MCMAC leads to higher TSC values because it forces a radial component into the merger rather than having a nonzero pericenter distance. This in turn increases the 3D separation of the subclusters and the TSC.

- Investigating merging clusters in the BigMDPL cosmological simulations, Wittman (2019) found

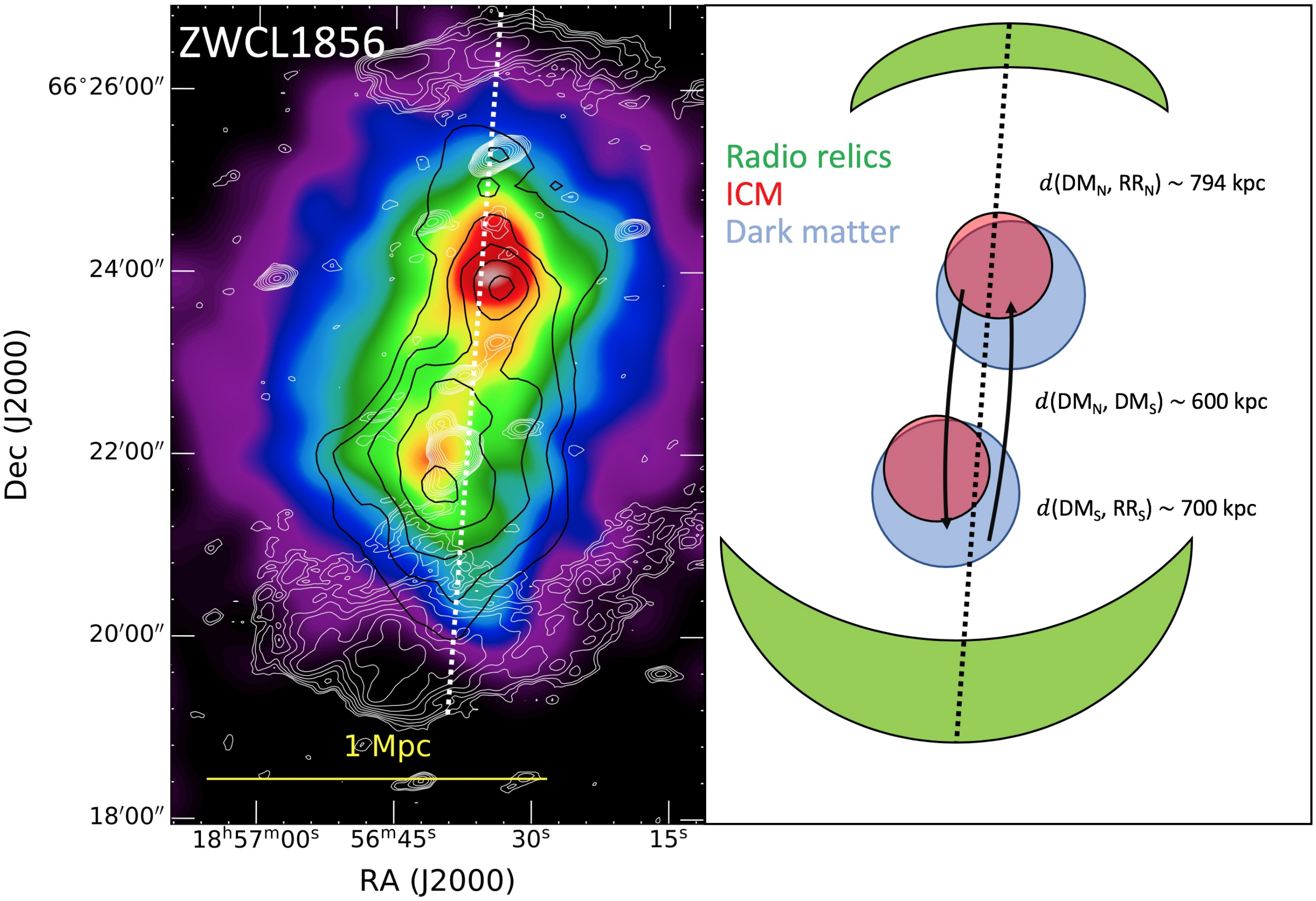

Figure 10. Left: XMM-*Newton* X-ray emission (0.5-7 keV) with LOFAR 144 MHz radio emission contours in white and WL mass contours in black. The mass peak in the north lies closer to the center of the cluster than the respective X-ray brightness peak. The white dotted line is our proposed merger axis. Right: Schematic of the merger scenario with measured distances.

that 68% (95%) of MACS1752 analogs have collision velocities ranging from 2444-3034 (1737-3264) km s^{-1}. This range of values is consistent with the value found from MCMAC. However, a major advantage of the analog method is that it can sample the collision velocity from the simulations, rather than infer it analytically. For this reason, we prefer the analog result. The analogs also provide a TSC for the system of 0.2-0.5 (0.1-1.1) Gyrs. The average TSC from the analogs is lower than that from MCMAC and is 2σ consistent. One of the disadvantages of the analog method (and MCMAC) is that it does not utilize the locations of the radio relics. In a merging cluster, the separation of the mass peaks is oscillates with time. Whereas, the shocks (radio relics) propagate unidirectionally and their separation is ever growing.

- The radio relics can also be used to approximate the collision speed by assuming the DSA model and converting the spectral indices to Mach numbers. Bonafede et al. (2012) reported injection spectral indices of 0.6 and 0.8, which give Mach numbers of 4.6 and 2.8 for the NE and SW radio relics, respectively. Unable to measure the X-ray temperature in the pre-shock region (outside the radio relic), we calculated the ICM sound speed from the global temperature (~5.9 keV) to be $c_s \sim 1200$ km s^{-1}. This should be taken as an upper limit on the sound speed assuming that the merger activity has inflated the temperature of the cluster. Ha et al. (2018) showed that axial shocks propagate at a nearly constant speed and Mach number from impact to 1 Mpc, which suggests that the shock Mach number may be a valid proxy for the collision speed. Thus, the expected collision velocity based on the Mach number of the radio relics is 5520 km s^{-1} for the NE relic and 3360 km s^{-1} for the SW. Both of these values are extremely high for a cluster merger. However, radio relics are known to have high Mach numbers, which may be caused by a preferential detection

Table 4. MCMAC input parameters

Parameter	Value	Uncertainty	Units
MACS1752			
$M_{\rm NE}$	5.6	1.7	10^{14} M$_\odot$
$M_{\rm SW}$	5.6	1.8	10^{14} M$_\odot$
$d_{\rm sep}$	1.2	0.1	Mpc
$z_{\rm NE}$	0.3648	0.0005	
$z_{\rm SW}$	0.3634	0.0005	
ZWCL1856			
$M_{\rm N}$	1.2	0.5	10^{14} M$_\odot$
$M_{\rm S}$	1.0	0.5	10^{14} M$_\odot$
d_{sep}	0.6	0.1	Mpc
$z_{\rm N}$	0.3041	0.0009	
$z_{\rm S}$	0.3033	0.0007	

of the highest Mach number region of the shock (Ha et al. 2018; van Weeren et al. 2019). Furthermore, a number of systematic effects may play a role (Stroe et al. 2014; van Weeren et al. 2016; Hoang et al. 2017). Although the velocities from the radio relics are high, we still provide TSC calculations based on them. Using the relic distance of 1.2 Mpc from barycenter, gives a TSC in the range 0.21 - 0.35 Gyrs.

5.2.2. *ZWCL1856*

ZWCL1856 (Figure 10) has a similar ICM morphology to MACS1752 with a bright region that runs between the subclusters. The ICM morphology does not show the distinct the ram-pressure stripped tails that MACS1752 has but the bright emission located between the subclusters could be from stripped gas. In comparison to MACS1752, the radio relics are better aligned with the elongation of the ICM. ZWCL1856 represents a cluster merger that the radio relics is a good proxy for the collision axis.

Our WL result portrays the merger as about 1:1 mass ratio but at a much lower total mass than MACS1752.

- The lower total mass is reflected in the MCMAC collision velocity of 1370^{+310}_{-179} km s^{-1}. MCMAC finds the TSC to be $0.63^{+0.24}_{-0.21}$ Gyrs. This TSC is lower than the value found for MACS1752 and is likely caused by the much smaller separation distance of the subclusters.

- The simulated analogs of Wittman (2019) prefer a collision velocity of 1494-1866 (1330-2094) km s^{-1} and a TSC of 0.3-0.5 (0.1-0.6) Gyrs. Both of these estimations are consistent with the MCMAC estimations.

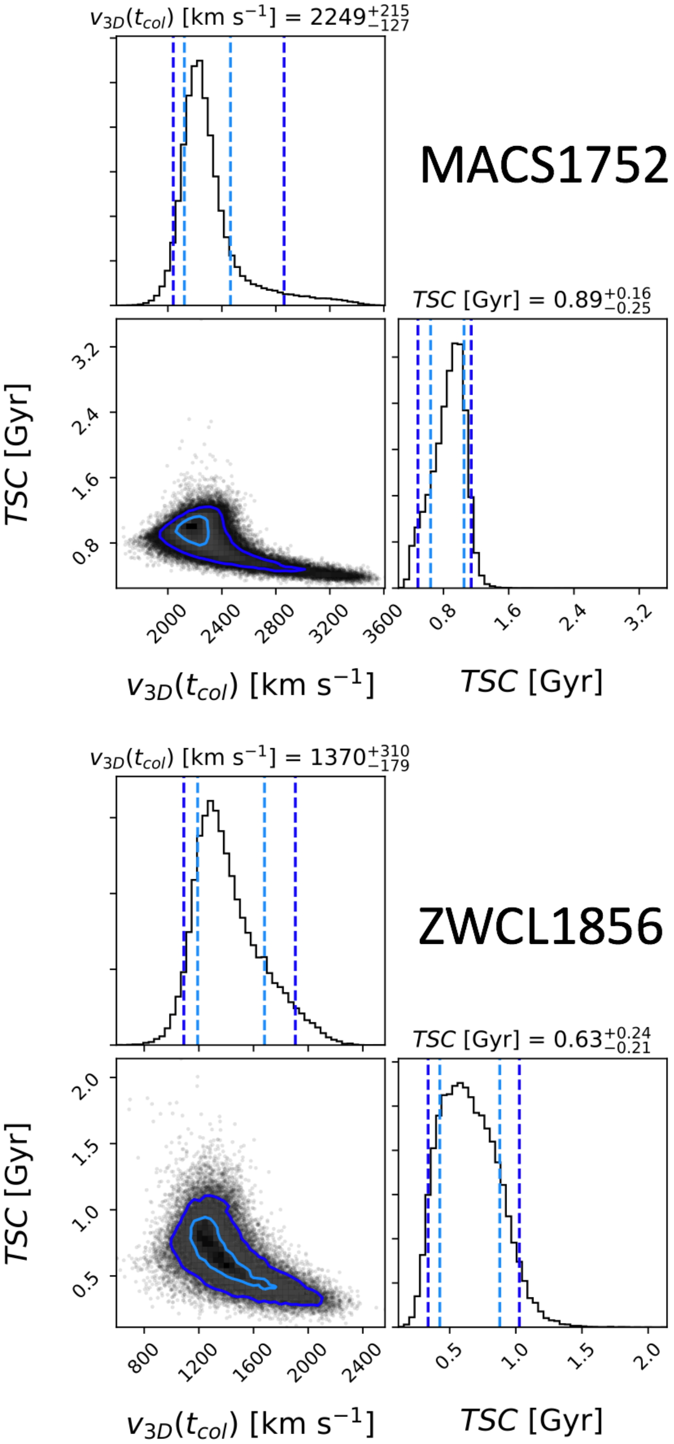

Figure 11. MCMAC results for MACS1752 (top) and ZWCL1856 (bottom). TSC is the time since collision and v_{3D} is the 3D velocity at the time of collision. Light blue lines denote the 1σ level and dark blue denote the 2σ level.

- From LOFAR, VLA, and GMRT radio observations, Jones et al. in prep. have derived integrated spectral indices of $\alpha_{\rm int} = -0.94 \pm 0.06$ and $\alpha_{\rm int} = -1.17 \pm 0.06$ for the N and S relics, respectively. An $\alpha_{\rm int} > -1$ is rare and, when converted to an injection index via $\alpha_{\rm inj} = \alpha_{\rm int} + 0.5$, is flatter than the DSA model allows. Alternatively, we may use the integrated spectral index of -0.94 ± 0.06 to find a lower bound for the Mach number. In that case, the lower bound for the Mach number is 2.4 for the N relic. Converting the S relic integrated spectral index to an injection index gives a Mach number of 3.6. Given a 3.7 keV plasma with a sound speed of ~1000 km s^{-1}, the collision velocity is $\gtrsim$ 2350 km s^{-1} and ~3600 km s^{-1} derived from the N and S relics, respectively. These give a range of TSC from 0.27-0.42 Gyrs for the relics at ~1 Mpc from barycenter.

MCMAC, simulated analogs, and the radio relics portray MACS1752 as a higher speed collision than ZWCL1856. This is in agreement with our expectation from the mass estimates. The TSC from the analogs and the radio relics predict that MACS1752 is a slightly younger merger than ZWCL1856. MCMAC predicts the opposite but we have discussed the pitfalls of MCMAC and the reasons that it can over predict the TSC.

5.2.3. *Comparing the Phases of MACS1752 and ZWCL1856*

The two clusters that we have analyzed in this work have remarkably similar features. Both are post-merger systems with double radio relics and bimodal mass distributions. Both systems have evidence of ICM interactions from a collision with a small but non-zero pericenter distance. However, an analysis of the differences will shed light on the merger phases.

An indication that ZWCL1856 is at a later stage of merging than MACS1752 comes from the comparison of the geometry of the systems. Assuming no projection effects (merger in the plane of the sky), we summarize the distances between the observed features of the clusters in Table 5. These measurements were made parallel to the defined collision axis (the white dotted lines in Figures 9 and 10). We define the ratio that compares the radio relic separation to the subcluster WL peaks separation as R2D (Table 5). R2D is a ratio that should almost always be increasing with time between first and second pericenter passage. Only in mergers that are observed near the radial direction from the observer and with a large impact parameter (ie. a large turn in the merger path) could the subclusters appear to outrun the radio relics and in that case it is expected that the radio relics would not be visible. The values of R2D that we have found for MACS1752 and ZWCL1856 are 1.9 and 3.5, respectively. The larger R2D of ZWCL1856 indicates that it is in a later stage of merging than MACS1752.

Table 5. Summary of Merger Properties

Parameter	Value	Units
MACS1752		
d(DM$_{\rm NE}$, DM$_{\rm SW}$)	1200	kpc
d(DM$_{\rm NE}$, RR$_{\rm NE}$)	715	kpc
d(DM$_{\rm SW}$, RR$_{\rm SW}$)	407	kpc
d(RR$_{\rm SW}$, RR$_{\rm NE}$)	2323	kpc
v_c	2444-3034	km s^{-1}
TSC	0.2-0.5	Gyrs
R2D	1.9	
ZWCL1856		
d(DM$_{\rm N}$, DM$_{\rm S}$)	600	kpc
d(DM$_{\rm N}$, RR$_{\rm N}$)	794	kpc
d(DM$_{\rm S}$, RR$_{\rm S}$)	700	kpc
d(RR$_{\rm S}$, RR$_{\rm N}$)	2094	kpc
v_c	1494-1866	km s^{-1}
TSC	0.3-0.5	Gyrs
R2D	3.5	

DM = dark matter peak (weak lensing)
RR = center of radio relic shock front
v_c and TSC are adopted from Wittman (2019) analogs
R2D is defined in Section 5.2.3

Another indication of the phase of the merger is the standoff distance (Verigin et al. 2003; Zhang et al. 2019), which compares the radius of a cold front to the separation distance of a shock from the stagnation point (leading edge of cold front / contact discontinuity). Unable to detect a cold front in the X-ray emission of ZWCL1856, we instead use the distance from the X-ray brightness peak to the radio relic as a proxy for standoff distance. The standoff distance of the ZWCL1856 relics are ~700 kpc and ~794 kpc. The NE relic of MACS1752 is ~715 kpc from its X-ray brightness peak and the SW relic is ~407 kpc. Given the same time interval, one would expect the radio relics of MACS1752 to separate more because of the larger impact velocity (shock speed). Since the relics of ZWCL1856 have a further standoff distance on average, we take this as another indication that ZWCL1856 is at a later stage of merging.

5.3. *Simulated Analogs from Literature*

An analog to MACS1752 was found in cosmological simulations by searching for X-ray features that resemble the XMM-*Newton* observations (Bonafede et al. 2012). Vazza et al. (2016) resimulated the cluster to study particle acceleration and found that the double relic configuration should be produced ~0.8 Gyrs after collision. The analog has a mass ~$6.5 \times 10^{14} M_{\odot}$ at redshift 0.3. This is about half the total mass that we have estimated for MACS1752. Nevertheless, visually comparing the simulated X-ray and radio emission of the analog to the observations presented here shows that the cluster merger is well reproduced. However, the symmetry is qualitatively better matched to ZWCL1856.

Skillman et al. (2013) presented another zoom-in simulation galaxy cluster merger that may be a candidate for MACS1752 or ZWCL1856. Their simulation showed a double relic cluster that appears to well represent the ICM features of ZWCL1856. In addition, they explored the effect that viewing angle would have on the radio relics by projecting the merger at various viewing angles. They were able to show that radio relics in clusters merging near a 45 degree angle to the sky were projected closer to the cluster center. However, the morphology of these projected relics did not have the uniform bow shock shape that the SW radio relic in MACS1752 has. For this reason, we suggest that projection is not the cause of the peculiar location of the SW radio relic in MACS1752.

5.4. *A Case for Non-thermal Particle Re-acceleration*

The rarity of radio relics in merging galaxy clusters and the inefficiency of DSA has led to the re-acceleration theory gaining popularity. Evidence for re-acceleration has been provided in work such as Bonafede et al. (2012) and van Weeren et al. (2017). In van Weeren et al. (2017), they show the clearest evidence for re-acceleration with a bridge connecting a nearby AGN to the radio relic.

The merger scenario that we have presented for MACS1752 is in slight tension with the position of the SW radio relic assuming that the relic should be visible off the bow of the subcluster. We theorize that this may be a case for re-acceleration of a non-thermal population of cosmic rays. Figure 5 in Bonafede et al. (2012) shows a connection between the cluster radio galaxy and radio relic in 323 MHz GMRT observations at the 3σ level. This bridge is also shown in the WSRT 18 cm contours in our Figure 9. A line from the barycenter of the merger to the center of the radio relic passes directly through this radio galaxy. We confirm that this galaxy is a cluster member at a redshift of 0.37086 ± 0.00002 from the Keck observations of Golovich et al. (2019a). In our merger scenario, the shock is launched along the collision axis in the direction of motion of the subcluster. We theorize that the south-west facing portion of the shock passed through the radio galaxy and has been re-accelerating the non-thermal electron population. Bonafede et al. (2012) presented a spectral index map of MASC1752 that shows a hint of a gradient that connects the radio galaxy to the radio relic but the evidence is not strong. New radio observations may provide the resolution to clearly see the spectral signature of a connection between the galaxy and the relic. In addition, deeper X-ray observations to search for the shock at the position of the radio relic and in front of the SW subcluster would be revealing.

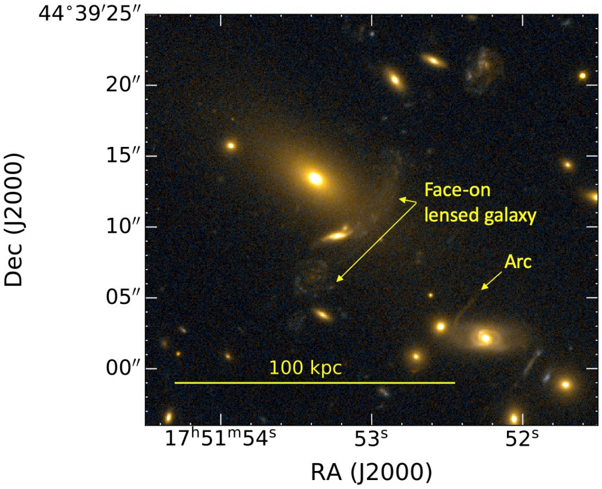

Figure 12. *HST* strong lens images near the SW BCG. A face-on spiral galaxy is seen close to the BCG with a cluster member galaxy partly obscuring the lens. An additional strong lens arc is found further to the southwest.

5.5. *HST strong lens images*

The *HST* deep imaging provides an opportunity to find strongly lensed galaxies in the vicinity of the MACS1752 subclusters. Figure 12 shows the region around the SW BCG with multiple lenses. Overlapping the inner region of the BCG, there is a lensed face-on spiral galaxy. This light is partially blocked by the cluster galaxy companion to the BCG. Located a bit further out is another strong arc. No counterpart to this arc is seen on the opposing side of the BCG. Future studies could model these features to constrain the small-scale mass distribution.

6. CONCLUSIONS

We have presented a weak-lensing and X-ray analysis of two double radio relic merging galaxy clusters: MACSJ1752.0+4440 and ZWCL1856.8+6616.

From our combined analysis of Subaru and *HST* observations, we have mapped the weak-lensing distribution of MACS1752 and found it to be dominated two subclusters. In addition, a low-mass substructure has been found between the subclusters. The mass peaks of these subclusters are consistent with the X-ray brightness and galaxy peaks. Modeling each subcluster with an NFW halo, we have concluded that the merger is 1:1 mass ratio with the NE (SW) subcluster mass being $M_{200} = 5.6^{+1.8}_{-1.6} \times 10^{14}$ M$_\odot$ ($M_{200} = 5.6^{+1.4}_{-2.1} \times 10^{14}$ M$_\odot$). We find the total mass to be $M_{200} = 14.7^{+3.8}_{-3.3} \times 10^{14}$ M$_\odot$. Our analysis of XMM-*Newton* X-ray observations show a ram-pressure stripped tail following the NE subcluster, which is interpreted as an indication of a nearly head-on collision. In addition, the ICM distribution is found to have an inverted S shape that connects the two subcluster centers. Defining the merger axis from the X-ray distribution, we have discovered that the SW radio relic is rotated from its expected position and may be a signature of particle re-acceleration in action.

Our weak-lensing analysis of Subaru imaging has found that ZWCL1856 is also a 1:1 mass ratio merger but at a much lower total mass than MACS1752. We estimate the mass of ZWCL1856 N (S) to be $M_{200} = 1.2 \pm 0.5 \times 10^{14}$ M$_\odot$ ($M_{200} = 1.0^{+0.4}_{-0.7} \times 10^{14}$ M$_\odot$) and total mass to be $M_{200} = 2.4^{+0.9}_{-0.7} \times 10^{14}$ M$_\odot$. Qualitatively, the X-ray emission and weak-lensing distribution of ZWCL1856 looks similar to MACS1752. The bright X-ray emission has the same inverted S shape that is found in MACS1752. In contrast to MACS1752, the merger axis for ZWCL1856 is well aligned with the elongated X-ray morphology, weak-lensing mass, and radio relics. Our tests show that the ZWCL1856 merger was a slower collision than that of MACS1752. Based on the ratio of radio relic separation to subcluster separation, we conclude that ZWCL1856 is in a later phase of merging than MACS1752.

Part of this work was performed under the auspices of the U.S. Department of Energy by Lawrence Livermore National Laboratory under Contract DE-AC52-07NA27344.

REFERENCES

Bell, A. R. 1978, MNRAS, 182, 443, doi: 10.1093/mnras/182.3.443

Bertin, E. 2006, in Astronomical Society of the Pacific Conference Series, Vol. 351, Astronomical Data Analysis Software and Systems XV, ed. C. Gabriel, C. Arviset, D. Ponz, & S. Enrique, 112

Bertin, E., & Arnouts, S. 1996, A&AS, 117, 393, doi: 10.1051/aas:1996164

Bertin, E., Mellier, Y., Radovich, M., et al. 2002, in Astronomical Society of the Pacific Conference Series, Vol. 281, Astronomical Data Analysis Software and Systems XI, ed. D. A. Bohlender, D. Durand, & T. H. Handley, 228

Bonafede, A., Intema, H. T., Brüggen, M., et al. 2014, ApJ, 785, 1, doi: 10.1088/0004-637X/785/1/1

Bonafede, A., Brüggen, M., van Weeren, R., et al. 2012, MNRAS, 426, 40, doi: 10.1111/j.1365-2966.2012.21570.x

Botteon, A., Brunetti, G., Ryu, D., & Roh, S. 2020, A&A, 634, A64, doi: 10.1051/0004-6361/201936216

Bradač, M., Allen, S. W., Treu, T., et al. 2008, ApJ, 687, 959, doi: 10.1086/591246

Carlberg, R. G., Yee, H. K. C., Ellingson, E., et al. 1996, ApJ, 462, 32, doi: 10.1086/177125

Chambers, K. C., Magnier, E. A., Metcalfe, N., et al. 2016, arXiv e-prints, arXiv:1612.05560. https://arxiv.org/abs/1612.05560

Dahlen, T., Mobasher, B., Dickinson, M., et al. 2010, The Astrophysical Journal, 724, 425. http://stacks.iop.org/0004-637X/724/i=1/a=425

Dawson, W. A. 2013, ApJ, 772, 131, doi: 10.1088/0004-637X/772/2/131

Dawson, W. A., Wittman, D., Jee, M. J., et al. 2012, ApJL, 747, L42, doi: 10.1088/2041-8205/747/2/L42

de Gasperin, F., van Weeren, R. J., Brüggen, M., et al. 2014, MNRAS, 444, 3130, doi: 10.1093/mnras/stu1658

Diemer, B., & Joyce, M. 2019, ApJ, 871, 168, doi: 10.3847/1538-4357/aafad6

Drury, L. O. 1983, Reports on Progress in Physics, 46, 973, doi: 10.1088/0034-4885/46/8/002

Duffy, A. R., Schaye, J., Kay, S. T., & Dalla Vecchia, C. 2008, MNRAS, 390, L64, doi: 10.1111/j.1745-3933.2008.00537.x

Ebeling, H., Edge, A. C., & Henry, J. P. 2001, ApJ, 553, 668, doi: 10.1086/320958

Eckert, D., Molendi, S., & Paltani, S. 2011, A&A, 526, A79, doi: 10.1051/0004-6361/201015856

Edge, A. C., Ebeling, H., Bremer, M., et al. 2003, MNRAS, 339, 913, doi: 10.1046/j.1365-8711.2003.06270.x

Feretti, L., Giovannini, G., Govoni, F., & Murgia, M. 2012, A&A Rv, 20, 54, doi: 10.1007/s00159-012-0054-z

Finner, K., Jee, M. J., Golovich, N., et al. 2017, ApJ, 851, 46, doi: 10.3847/1538-4357/aa998c

Fischer, P., & Tyson, J. A. 1997, AJ, 114, 14, doi: 10.1086/118447

Ghizzardi, S., Rossetti, M., & Molendi, S. 2010, A&A, 516, A32, doi: 10.1051/0004-6361/200912496

Girardi, M., Manzato, P., Mezzetti, M., Giuricin, G., & Limboz, F. 2002, ApJ, 569, 720, doi: 10.1086/339360

Golovich, N., Dawson, W. A., Wittman, D. M., et al. 2019a, ApJ, 882, 69, doi: 10.3847/1538-4357/ab2f90

—. 2019b, ApJS, 240, 39, doi: 10.3847/1538-4365/aaf88b

Gu, L., Akamatsu, H., Shimwell, T. W., et al. 2019, Nature Astronomy, 3, 838, doi: 10.1038/s41550-019-0798-8

Ha, J.-H., Ryu, D., & Kang, H. 2018, ApJ, 857, 26, doi: 10.3847/1538-4357/aab4a2

HI4PI Collaboration, Ben Bekhti, N., Flöer, L., et al. 2016, A&A, 594, A116, doi: 10.1051/0004-6361/201629178

Hoang, D. N., Shimwell, T. W., Stroe, A., et al. 2017, MNRAS, 471, 1107, doi: 10.1093/mnras/stx1645

Hoekstra, H., Franx, M., & Kuijken, K. 2000, ApJ, 532, 88, doi: 10.1086/308556

Jee, M. J., Blakeslee, J. P., Sirianni, M., et al. 2007, PASP, 119, 1403, doi: 10.1086/524849

Jee, M. J., Hughes, J. P., Menanteau, F., et al. 2014, ApJ, 785, 20, doi: 10.1088/0004-637X/785/1/20

Jee, M. J., Mahdavi, A., Hoekstra, H., et al. 2012, ApJ, 747, 96, doi: 10.1088/0004-637X/747/2/96

Jee, M. J., Tyson, J. A., Schneider, M. D., et al. 2013, ApJ, 765, 74, doi: 10.1088/0004-637X/765/1/74

Jee, M. J., Dawson, K. S., Hoekstra, H., et al. 2011, ApJ, 737, 59, doi: 10.1088/0004-637X/737/2/59

Kang, H., & Jones, T. W. 2005, ApJ, 620, 44, doi: 10.1086/426855

Kang, H., & Ryu, D. 2011, ApJ, 734, 18, doi: 10.1088/0004-637X/734/1/18

Kang, H., Ryu, D., & Jones, T. W. 2012, ApJ, 756, 97, doi: 10.1088/0004-637X/756/1/97

Koekemoer, A. M., Fruchter, A. S., Hook, R. N., & Hack, W. 2003, in HST Calibration Workshop : Hubble after the Installation of the ACS and the NICMOS Cooling System, 337

Lee, W., Jee, M. J., Kang, H., et al. 2020, ApJ, 894, 60, doi: 10.3847/1538-4357/ab855f

Malkov, M. A., & Drury, L. O. 2001, Reports on Progress in Physics, 64, 429, doi: 10.1088/0034-4885/64/4/201

Mandelbaum, R. 2018, ARA&A, 56, 393, doi: 10.1146/annurev-astro-081817-051928

Mandelbaum, R., Rowe, B., Armstrong, R., et al. 2015, MNRAS, 450, 2963, doi: 10.1093/mnras/stv781

Markevitch, M., Gonzalez, A. H., Clowe, D., et al. 2004, ApJ, 606, 819, doi: 10.1086/383178

Markevitch, M., Gonzalez, A. H., David, L., et al. 2002, ApJL, 567, L27, doi: 10.1086/339619

Markevitch, M., & Vikhlinin, A. 2007, PhR, 443, 1, doi: 10.1016/j.physrep.2007.01.001

Navarro, J. F., Frenk, C. S., & White, S. D. M. 1997, ApJ, 490, 493, doi: 10.1086/304888

Ogrean, G. A., Brüggen, M., Röttgering, H., et al. 2013a, MNRAS, 429, 2617, doi: 10.1093/mnras/sts538

Ogrean, G. A., Brüggen, M., van Weeren, R. J., et al. 2013b, MNRAS, 433, 812, doi: 10.1093/mnras/stt776

Okabe, N., & Smith, G. P. 2016, MNRAS, 461, 3794, doi: 10.1093/mnras/stw1539

Ouchi, M., Shimasaku, K., Okamura, S., et al. 2004, ApJ, 611, 660, doi: 10.1086/422207

Pinzke, A., Oh, S. P., & Pfrommer, C. 2013, MNRAS, 435, 1061, doi: 10.1093/mnras/stt1308

Planck Collaboration, Ade, P. A. R., Aghanim, N., et al. 2016, A&A, 594, A27, doi: 10.1051/0004-6361/201525823

Randall, S. W., Clarke, T. E., van Weeren, R. J., et al. 2016, ApJ, 823, 94, doi: 10.3847/0004-637X/823/2/94

Rengelink, R. B., Tang, Y., de Bruyn, A. G., et al. 1997, A&AS, 124, 259, doi: 10.1051/aas:1997358

Ricker, P. M. 1998, ApJ, 496, 670, doi: 10.1086/305393

Ricker, P. M., & Sarazin, C. L. 2001, ApJ, 561, 621, doi: 10.1086/323365

Sarazin, C. L. 2002, Astrophysics and Space Science Library, Vol. 272, The Physics of Cluster Mergers, ed. L. Feretti, I. M. Gioia, & G. Giovannini, 1–38, doi: 10.1007/0-306-48096-4_1

Schrabback, T., Applegate, D., Dietrich, J. P., et al. 2018, MNRAS, 474, 2635, doi: 10.1093/mnras/stx2666

Seitz, C., & Schneider, P. 1997, A&A, 318, 687. https://arxiv.org/abs/astro-ph/9601079

Sirianni, M., Jee, M. J., Benítez, N., et al. 2005, PASP, 117, 1049, doi: 10.1086/444553

Skillman, S. W., Xu, H., Hallman, E. J., et al. 2013, ApJ, 765, 21, doi: 10.1088/0004-637X/765/1/21

Stroe, A., Harwood, J. J., Hardcastle, M. J., & Röttgering, H. J. A. 2014, MNRAS, 445, 1213, doi: 10.1093/mnras/stu1839

van Weeren, R. J., Bonafede, A., Ebeling, H., et al. 2012, MNRAS, 425, L36, doi: 10.1111/j.1745-3933.2012.01301.x

van Weeren, R. J., de Gasperin, F., Akamatsu, H., et al. 2019, SSRv, 215, 16, doi: 10.1007/s11214-019-0584-z

van Weeren, R. J., Brunetti, G., Brüggen, M., et al. 2016, ApJ, 818, 204, doi: 10.3847/0004-637X/818/2/204

van Weeren, R. J., Andrade-Santos, F., Dawson, W. A., et al. 2017, Nature Astronomy, 1, 0005, doi: 10.1038/s41550-016-0005

Vazza, F., Brüggen, M., Wittor, D., et al. 2016, MNRAS, 459, 70, doi: 10.1093/mnras/stw584

Vazza, F., Eckert, D., Brüggen, M., & Huber, B. 2015, MNRAS, 451, 2198, doi: 10.1093/mnras/stv1072

Verigin, M., Slavin, J., Szabo, A., et al. 2003, Journal of Geophysical Research (Space Physics), 108, 1323, doi: 10.1029/2002JA009711

Voges, W., Aschenbach, B., Boller, T., et al. 1999, A&A, 349, 389. https://arxiv.org/abs/astro-ph/9909315

Wittman, D. 2019, ApJ, 881, 121, doi: 10.3847/1538-4357/ab3052

Wright, C. O., & Brainerd, T. G. 2000, ApJ, 534, 34, doi: 10.1086/308744

Yagi, M., Kashikawa, N., Sekiguchi, M., et al. 2002, AJ, 123, 66, doi: 10.1086/324731

Zhang, C., Churazov, E., Forman, W. R., & Jones, C. 2019, MNRAS, 482, 20, doi: 10.1093/mnras/sty2501

ZuHone, J. A. 2011, ApJ, 728, 54, doi: 10.1088/0004-637X/728/1/54

Zwicky, F., Herzog, E., Wild, P., Karpowicz, M., & Kowal, C. T. 1961, Catalogue of galaxies and of clusters of galaxies, Vol. I